



**UNIVERSIDAD DE INVESTIGACIÓN DE TECNOLOGÍA
EXPERIMENTAL YACHAY**

Escuela de Ciencias de la Tierra, Energía y Ambiente

**TÍTULO: Spatial analysis of a critical slope instability area through
multitemporal UAV photogrammetry.**

Trabajo de integración curricular presentado como requisito para la
obtención del título de Geólogo

Autor:

Anderson Patricio Rivadeneira Aguirre

Tutor:

PhD – Elisa Piispa

Urcuquí, 9 de julio de 2021

SECRETARÍA GENERAL
(Vicerrectorado Académico/Cancillería)
ESCUELA DE CIENCIAS DE LA TIERRA, ENERGÍA Y AMBIENTE
CARRERA DE GEOLOGÍA
ACTA DE DEFENSA No. UITEY-GEO-2021-00008-AD

A los 9 días del mes de julio de 2021, a las 09:00 horas, de manera virtual mediante videoconferencia, y ante el Tribunal Calificador, integrado por los docentes:

Presidente Tribunal de Defensa	Dr. ALMEIDA GONZALEZ, RAFAEL VLADIMIR , Ph.D.
Miembro No Tutor	Dra. FOSTER ANNA ELIZABETH , Ph.D.
Tutor	Dra. PIISPA , ELISA JOHANNA , Ph.D.

El(la) señor(ita) estudiante **RIVADENEIRA AGUIRRE, ANDERSON PATRICIO**, con cédula de identidad No. **0401926100**, de la **ESCUELA DE CIENCIAS DE LA TIERRA, ENERGÍA Y AMBIENTE**, de la Carrera de **GEOLOGÍA**, aprobada por el Consejo de Educación Superior (CES), mediante Resolución **RPC-SE-10-No.031-2016**, realiza a través de videoconferencia, la sustentación de su trabajo de titulación denominado: **Spatial analysis of a critical slope instability area through multitemporal UAV photogrammetry** , previa a la obtención del título de **GEÓLOGO/A**.

El citado trabajo de titulación, fue debidamente aprobado por el(los) docente(s):

Tutor	Dra. PIISPA , ELISA JOHANNA , Ph.D.
--------------	-------------------------------------

Y recibió las observaciones de los otros miembros del Tribunal Calificador, las mismas que han sido incorporadas por el(la) estudiante.

Previamente cumplidos los requisitos legales y reglamentarios, el trabajo de titulación fue sustentado por el(la) estudiante y examinado por los miembros del Tribunal Calificador. Escuchada la sustentación del trabajo de titulación a través de videoconferencia, que integró la exposición de el(la) estudiante sobre el contenido de la misma y las preguntas formuladas por los miembros del Tribunal, se califica la sustentación del trabajo de titulación con las siguientes calificaciones:

Tipo	Docente	Calificación
Presidente Tribunal De Defensa	Dr. ALMEIDA GONZALEZ, RAFAEL VLADIMIR , Ph.D.	8,2
Tutor	Dra. PIISPA , ELISA JOHANNA , Ph.D.	8,8
Miembro Tribunal De Defensa	Dra. FOSTER ANNA ELIZABETH , Ph.D.	8,2

Lo que da un promedio de: **8.4 (Ocho punto Cuatro)**, sobre 10 (diez), equivalente a: **APROBADO**

Para constancia de lo actuado, firman los miembros del Tribunal Calificador, el/la estudiante y el/la secretario ad-hoc.

RIVADENEIRA AGUIRRE, ANDERSON PATRICIO
Estudiante



Dr. ALMEIDA GONZALEZ, RAFAEL VLADIMIR , Ph.D.
Presidente Tribunal de Defensa

RAFAEL VLADIMIR
ALMEIDA
GONZALEZ

Digitally signed by RAFAEL VLADIMIR ALMEIDA GONZALEZ
 DN: cn=RAFAEL VLADIMIR ALMEIDA GONZALEZ, serialNumber=211020132449, ou=ENTIDAD DE CERTIFICACION DE INFORMACION, o=SECURITY DATA S.A. 2, c=EC
 Date: 2021.07.10 23:47:07 -05'00'

Dra. PIISPA , ELISA JOHANNA , Ph.D.
Tutor

Digitally signed by ELISA JOHANNA PIISPA

Dra. FOSTER ANNA ELIZABETH , Ph.D.
Miembro No Tutor

ANNA
ELIZABETH
FOSTER

Digitally signed by ANNA ELIZABETH FOSTER
 Date: 2021.07.09 13:43:21 -05'00'

TERÁN ROSALES, ANDREA YOLANDA
Secretario Ad-hoc

ANDREA
YOLANDA
TERAN ROSALES
Firmado digitalmente por
ANDREA YOLANDA
TERAN ROSALES
Fecha: 2021.07.09
11:36:23 -05'00'

AUTORÍA

Yo, **Anderson Patricio Rivadeneira Aguirre**, con cédula de identidad 0401926100, declaro que las ideas, juicios, valoraciones, interpretaciones, consultas bibliográficas, definiciones y conceptualizaciones expuestas en el presente trabajo; así cómo, los procedimientos y herramientas utilizadas en la investigación, son de absoluta responsabilidad de el/la autora (a) del trabajo de integración curricular. Así mismo, me acojo a los reglamentos internos de la Universidad de Investigación de Tecnología Experimental Yachay

Urcuquí, Julio 2021.



Anderson Patricio Rivadeneira

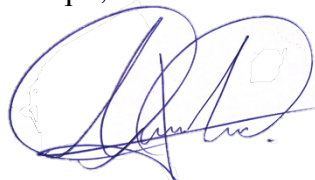
CI: 0401926100

AUTORIZACION DE PUBLICACIÓN

Yo, **Anderson Patricio Rivadeneira Aguirre**, con cédula de identidad 0401926100, cedo a la Universidad de Investigación de Tecnología Experimental Yachay, los derechos de publicación de la presente obra, sin que deba haber un reconocimiento económico por este concepto. Declaro además que el texto del presente trabajo de titulación no podrá ser cedido a ninguna empresa editorial para su publicación u otros fines, sin contar previamente con la autorización escrita de la Universidad.

Asimismo, autorizo a la Universidad que realice la digitalización y publicación de este trabajo de integración curricular en el repositorio virtual, de conformidad a lo dispuesto en el Art. 144 de la Ley Orgánica de Educación Superior.

Urququí, Julio 2021.



Anderson Patricio Rivadeneira

CI: 0401926100

ABSTRACT (341 words)

Recent years have seen a rapid worldwide rise in the vulnerability to natural hazards that affect humans. Inadequate government regulations and ineffective implementation of territorial planning policies result in frequent construction of buildings in marginal and high-risk areas to natural hazards. One of these wrong decisions is the expansion of semi-urban settlements in areas susceptible to slope failure. In the present study, geomatic approaches to assess volumetric and topography changes over time were implemented in an area of critical slope instability at the northwest outskirts of the city of Urcuquí, Ecuador. The methodology applied allowed recording spatial changes in the soil surface topography over an area of approximately 0.171 km² over a period of ~6 months (October 2020 to March 2021). The main equipment used to acquire the data was a DJI Inspire 2 unmanned aerial vehicle. From the aerial photogrammetry data processed with Structure from Motion software Pix4D Mapper dense point clouds at high resolution (0.5 to 4 cm/pixel) were generated, which were our data base for the development of the study. Our results from spatial analysis show that the slope undergoes a continuous change during the period of study. Results of the C2M and M3C2 comparisons in Cloud Compare software show critical regions of constant movement and slope failure in the two sides of the Pinchinguela ravine in which the study was developed. However, it is not possible to reach the resolution of millimeters which was obtained to describe the 3D vectors motion obtained from ground control points data by traditional topographic surveys with Trimble Total Station S5. Even though the identified slope instability area showed specific sections of slope failure and displacements, it can result in a catastrophic event if the Municipal Autonomous Decentralized Government of San Miguel of Urcuquí does not apply any kind of planning and territorial measurements to mitigate this hazard. Finally, the methodology of this study can be used to risk detection of any type of mass movements as well as land use planning in semi-urban settlements in Ecuador and the rest of the world.

KEYWORDS: Vulnerability, semi-urban settlements, slope instability areas, aerial photogrammetry technique, risk detection method.

RESUMEN (378 palabras)

En los últimos años se ha observado un incremento sustancial a nivel mundial de la vulnerabilidad ante los desastres naturales que afectan a los seres humanos. Las inadecuadas regulaciones gubernamentales y la ineficaz implementación de políticas de planificación territorial han dado por resultado una frecuente construcción de edificaciones en áreas marginales y de alto riesgo frente amenazas naturales. Una de estas decisiones equivocadas es la expansión de asentamientos semiurbanos en áreas susceptibles a deslizamientos de ladera. En el presente estudio, se implementó un enfoque geomático para evaluar cambios volumétricos y topográficos a lo largo del tiempo en un área que presenta inestabilidad en sus taludes, localizada en las afueras del noroeste de la ciudad de Urcuquí, Ecuador. La metodología aplicada permitió registrar cambios espaciales en la topografía de la superficie del suelo en un área de aproximadamente 0.171 km² durante un período de ~6 meses (Octubre 2020 a Marzo 2021). El principal equipo utilizado para adquirir los datos fue un vehículo aéreo no tripulado, DJI Inspire 2. A partir de la fotogrametría aérea procesada con el SfM software Pix4D Mapper se generaron nubes de puntos densas de alta resolución (0,5 a 4 cm / píxel), las cuales fueron la información base para el desarrollo del estudio. Los resultados del análisis espacial muestran que la pendiente presenta un cambio continuo durante el período de estudio. Los resultados de las comparaciones usando los algoritmos C2M y M3C2 en el software Cloud Compare muestran regiones críticas de movimiento constante y fallas de pendiente en los dos lados de la quebrada Pinchinguela. Sin embargo, no es posible alcanzar la resolución milimétrica que se obtuvo para describir el movimiento de los vectores 3D, obtenidos a partir de los datos de los puntos de control terrestre mediante levantamientos topográficos tradicionales con la estación total Trimble S5. Si bien el área de taludes identificada identificado mostro áreas específicas de fallas y desplazamientos, puede resultar en un evento catastrófico si el Gobierno Autónomo Descentralizado Municipal de San Miguel de Urcuquí no implementa ningún tipo de planificación y restricciones territoriales para mitigar este peligro. Finalmente, la metodología de este estudio se puede utilizar como método de detección de riesgos de deslizamientos de tierra y planificación del uso del suelo en asentamientos semiurbanos en Ecuador y el resto del mundo.

PALABRAS CLAVE: Vulnerabilidad, asentamientos semiurbanos, pendientes inestables, fotogrametría aérea, método de detección de riesgos.

TABLE OF CONTENTS

ABSTRACT	6
INTRODUCTION AND JUSTIFICATION	11
PROBLEM STATEMENT	13
OBJECTIVES	14
SPECIFIC OBJECTIVES	14
STUDY AREA.....	15
METHODS.....	21
UAV Photogrammetry	21
Double Grid Constant Elevation Capturing Mode	22
Terrain Awareness Capturing Mode.....	22
Traditional Topography	23
Ground Control Points	23
Data Processing.....	24
Processing of point cloud raw data	26
Spatial Analysis	26
Three-dimensional Comparison.....	27
Two-dimensional comparison	31
RESULTS.....	32
Cloud to Mesh Comparison results	35
Multiscale Model to Model Cloud Comparison results	37
3D Vector motions	40
Profiles.....	41
DISCUSSION	44
CONCLUSIONS.....	51
REFERENCES.....	52
ANNEXES	58

LIST OF TABLES

Table 1: Socioeconomic standing of Urcuquí population.....	18
Table 2: Average GSD obtained from UAV-SfM process.	33
Table 3: Information related to the UAV campaigns and processing on Pix4D Mapper.	34
Table 4: Absolute geolocation variation (Root Mean Square Error).	34
Table 5: Final RMSE values corresponding to the ICP alignment on Cloud Compare software.	35

LIST OF FIGURES

Figure 1: Location of the study area.....	15
Figure 2. Aerial image of the study area with slope steepness superimposed on the map.	16
Figure 3. Stratigraphic column correlated to a panoramic image of the study area.....	17
Figure 4. Weather archive Urcuquí.	18
Figure 5. Urcuquí urbanization trend.	19
Figure 6. Panoramic images of the study area.	20
Figure 7. Workflow diagram of the study methodology.....	21
Figure 8. GCPs distribution and Total Station locations.....	24
Figure 9. Illustration of the difference between both C2C distances and C2M distance	28
Figure 10. Illustration of the two steps of the M3C2 comparison process and the function on complex topography.	29
Figure 11. Orthophotos obtained from the UAV-SfM process.....	32
Figure 12. Cloud to mesh distance values in meters between October to December 2020	36
Figure 13. Cloud to mesh distance values in meters between October 2020 to March 2021.	36
Figure 14. M3C2 distance calculation between the October 2020 to March 2021 surveys of the filling part with the respectively Gaussian plot; highlighting the most critical areas of remotion of material.	38
Figure 15. M3C2 distance calculation between the October 2020 to March 2021 surveys of the front part with the respectively Gaussian plot; highlighting the most critical areas of remotion of material.	38
Figure 16. Critical areas of remotion within the front slope.	39
Figure 17. Displacement vectors from the GCPs data, derived from traditional topography surveys since December 2020 to March 2021.	41
Figure 18. Profile along the North. Cross sections concerning October, December, March.....	42
Figure 19. South profile. October, December, March.....	43

INTRODUCTION AND JUSTIFICATION

As a consequence of demographic growth, humans are currently more exposed to natural hazards. One of the main factors that has increased human vulnerability to natural hazards is the high demand for housing in recent years (UNDESA, 2016). In Ecuador, the migration from rural to urban areas in order to search for a better life and more opportunities has become very common. The migration process is not only towards the main cities, but also occurs toward the central areas of each canton, generating urban agglomerations. Therefore, the displaced population settle in the outskirts of each urban area, forming the so-called semi-urban settlements (Zapata et al., 2019).

The urban zone of Urcuquí canton shows a population growth of around 16% between 2001 to 2010 (GADMU, 2015). The population has low levels of education, literacy, and widespread job insecurity. Due to these reasons, the most common economic activities undertaken in the area are agriculture, cattle raising, and forestry on a small scale (INEC, 2010). The high price of land in the mostly flat urban area causes the infrastructural development of the canton to be directed towards the steep slopes that surround it (GADMU, 2015). Unfortunately, many sectors surrounding these steep slopes, including an area called El Rosario, experience a high level of vulnerability to natural hazards like mass movements (Gobierno Provincial de Imbabura, 2015).

Slope stability analysis is a technique for evaluating and estimating slope displacements. It allows quantification of the spatial and temporal evolution of a slope, which constitutes a fundamental method for urban planning and risk management. Currently, several geomatic techniques can be used to reconstruct the three-dimensional shape of an area at a high level of accuracy such as Global Navigation Satellite System (GNSS), Synthetic Aperture Radar (SAR), Laser imaging Detection and Ranging (LIDAR), Unmanned Aerial Vehicle (UAV), Terrestrial Laser Scanner (TLS), among others (Arif et al., 2018; Borgatti et al., 2010; He & Heki, 2018; Kerle et al., 2019; Williams et al., 2020).

Photogrammetry based on Unmanned Aerial Vehicles is a potential cost-effective and efficient alternative to acquire two dimensional images of any type of surface, where images are taken from different angles and distances using flight plan modes (Boon et al., 2016; Nex & Remondino, 2014). UAV photogrammetry data processed with Structure from Motion (SfM) software allow

the automatic orientation, detection and matching of features on the obtained images, and to triangulate positions within a defined 3D coordinate system (Peterson et al., 2015). Furthermore, UAV data from SfM processing enables the construction of three-dimensional models of a surface (Westoby et al., 2012). However, the resolution and accuracy of the results obtained from aerial photogrammetry techniques depend on various external and internal factors, such as camera calibration, focal length and the use of ground control points (GCPs) and the settings used in the postprocessing of SfM images (Agüera et al., 2017; Kameyama & Sugiura, 2021; Sanz et al., 2018)

The main objective of this study is to characterize the slope instability in the development area of Urcuquí City by analyzing volumetric changes over time. This will be done with two-dimensional and three-dimensional comparisons of the data obtained from UAV-SfM derived products. Previous studies have applied the UAV-SfM methodology to other natural hazards like mudslides, rock failures, volcanic eruptions, and others e.g. (Giuseppe Esposito et al., 2017; Kameyama & Sugiura, 2021; Kerle et al., 2019; Mlambo et al., 2017). Therefore, the data generated with this methodology can serve as primary information in making decisions to prevent, control, and mitigate natural disasters.

PROBLEM STATEMENT

Some of the main challenges faced by land use planners and risk managers in Ecuador come from the accelerated changes in the demographic structure of the region. As the population grows, the land surface is covered by human settlements, but this land in some cases is vulnerable to slope failure. Moreover, anthropogenic activities, such as the expansion of agricultural activities, water runoff from unplanned constructions, and soil movement for the development of infrastructure, lead to alterations in the stability of slopes. Above all, it affects areas where the soils are not well consolidated, or where any type of natural destabilization process is already promoting further slope failure.

For these reasons, it is crucial to know the factors involved in slope stability and understand the interactions between them. The areas of greatest susceptibility to slope failure should be identified and the mitigation, correction, and protection measures implemented. In this case study we focus on the first aspect, identifying areas susceptible to slope failure in the northwest of Urcuquí on a portion of the Pinchinguela ravine. In this area the vulnerability to building collapses of the preexisting constructions and any future infrastructures is high, mainly by the morphological features observed which are related to mass movements in the past.

Our aim is to develop an accessible method to provide several numerical and graphic products based on spatial analysis using UAV photogrammetry and explore the benefits that can be obtained by incorporating different Structure from Motion (SfM) techniques to have a comprehensive database required for spatial analysis of slope instability areas. The data obtained allow us to describe the morphological changes that occurred during the study period. The method could be implemented as a part of any risk management plan that municipalities can apply without a large investment or training of the operators.

OBJECTIVES

Our main objective is to detect and monitor spatial changes in the soil surface topography of a potential slope instability area located in the Northwest of the Urcuquí City.

SPECIFIC OBJECTIVES

To generate UAV-SfM derived products with a reasonable level of accuracy.

To describe graphically the variation of morphological changes using the UAV-SfM derived products.

To describe numerically specific vector motions using the GCP data obtained through traditional topographical surveys.

To test and develop further an accurate non-contact slope instability identification method for high-risk areas.

STUDY AREA

The study was carried out on an area located in the northern Ecuadorian highlands, Imbabura province, San Miguel de Urucuquí canton. The area surrounds the Pinchinguela ravine, which is the limit between the San Blas and Urucuquí cities (Fig. 1). However, most of the study area is considered belonging to Urucuquí city because that side of the stream is designated for construction and the land surface part of San Blas is an area dedicated for growing pine.

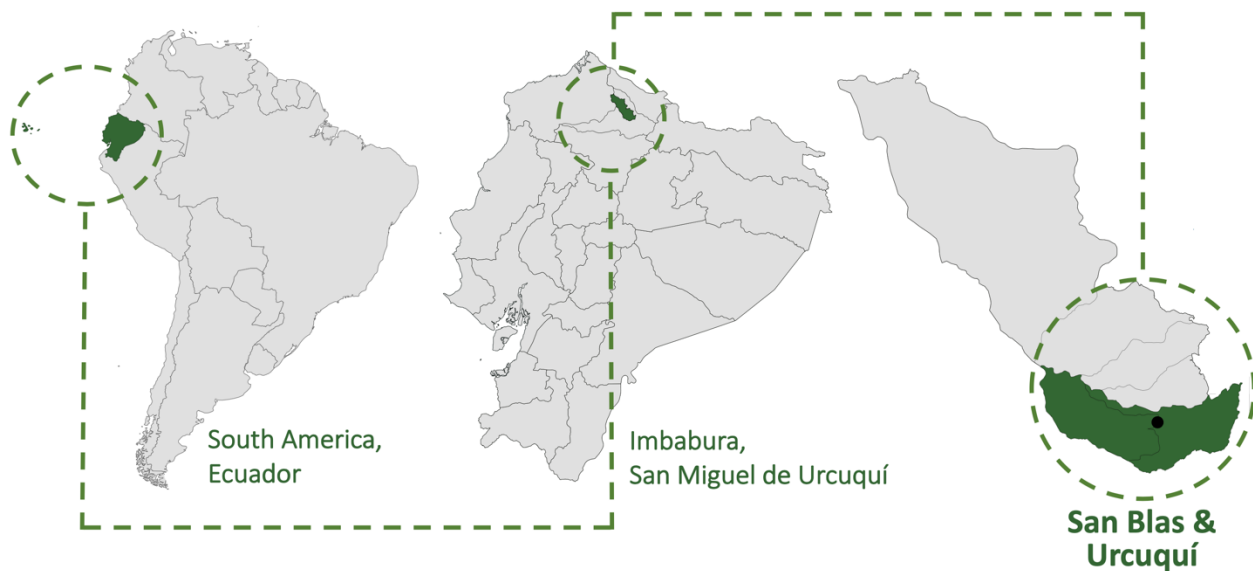


Figure 1. Location of the study area.

Our case study covers an area of nearly 0.171 km² at around 2300 meters above sea level. In the Pinchinguela ravine the elevation changes are very pronounced, with many slopes greater than 70 degrees, and average of about 40 degrees (Fig. 2). The study area consists of different slope classes and the elevation range is about 150 m.

Regarding geology, the main lithological composition in the area is a sequence of volcanic products associated with the two main eruptive events of the Chachimbiro volcano over the Yanahurco Formation (Beate & Urquizo, 2015). In Figure 3 we show an extract of the corresponding stratigraphic column, which underlines the sequences of primary volcanic deposits: massive fine ash, massive coarse ash, massive clast supported lapilli, massive clast supported lapilli to block, matrix supported ash to lapilli, massive clast supported ash to lapilli and undefined lithology.

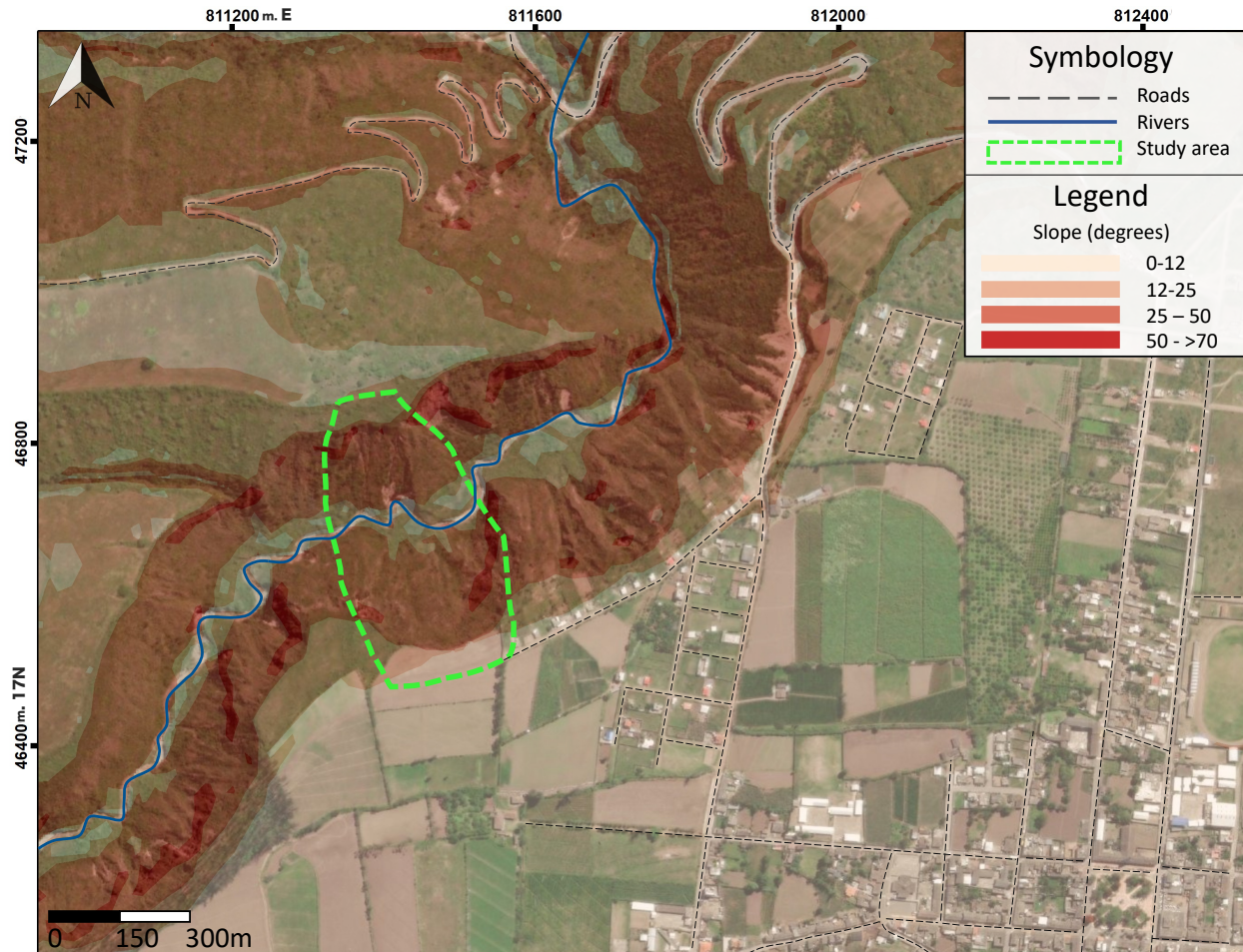


Figure 2. Aerial image of the study area near the growth zone of the City of Urucuquí with slope steepness superimposed on the same map.

From a hydrographic point of view, as mentioned before the Pinchinguela ravine limits the area. However, the underground flow within the ravine is minimal, and considerable only in some days during the winter season. According to records obtained from 1979 to 2015 by the National Institute of Meteorology and Hydrology (INAMHI), Urucuquí canton return periods of maximum monthly rainfall occur during the months of April and November (Plan de Desarrollo y Ordenamiento Territorial de San Miguel de Urucuquí, 2014). However, due to the location of the mountain range's eastern and western foothills, the inter-Andean valleys, and relief characteristics, rainfall is dispersed across the orography, resulting in significant variations of the amount of rain over short distances. Also, it should be emphasized that there is no meteorological station in Urucuquí city. The data mentioned above belongs to the records of the meteorological station

located in Cahuasquí. However, simulated meteorological data can be obtained from Meteoblue® for the selected area (Fig. 4).

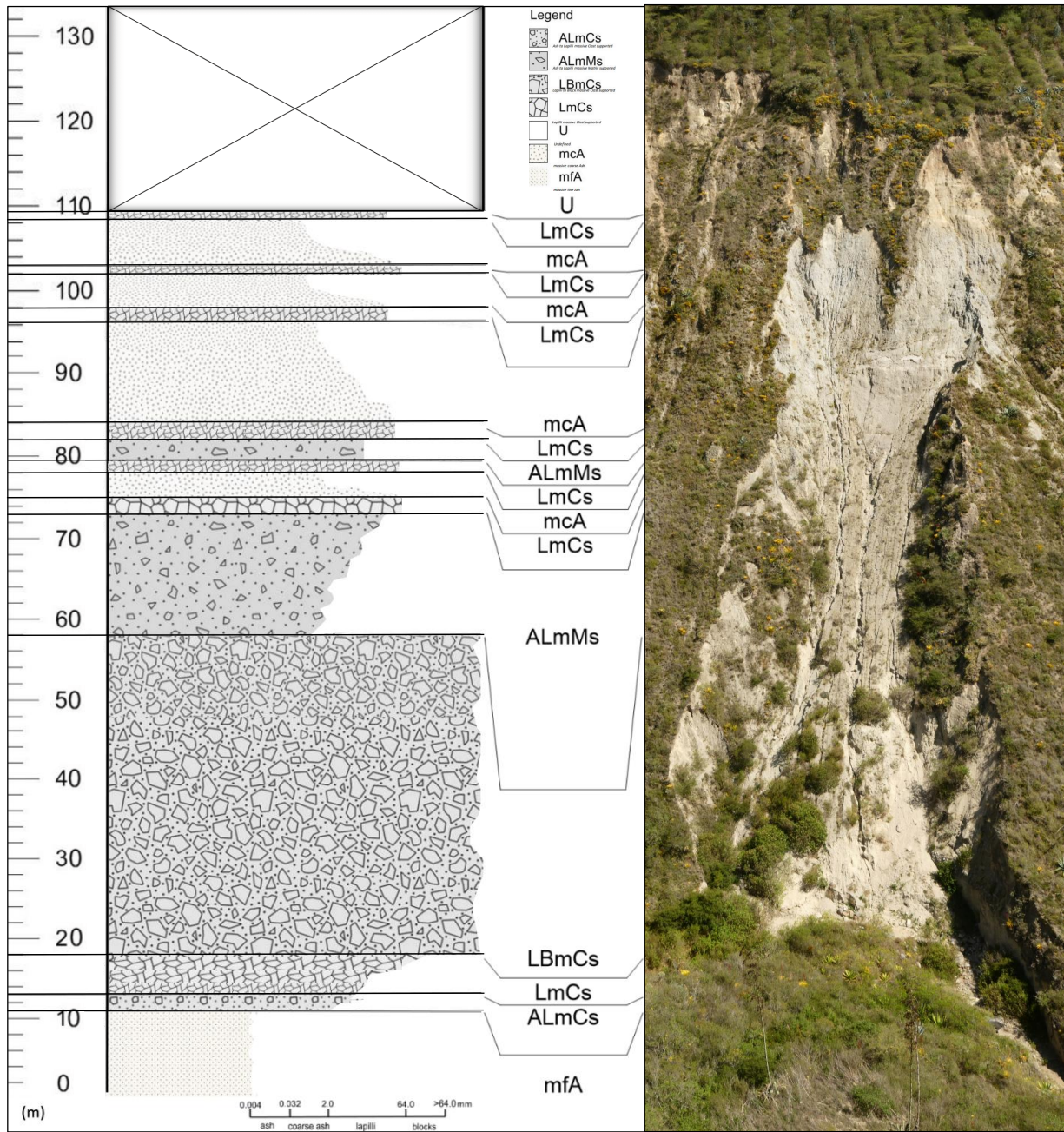


Figure 3. Stratigraphic column correlated to a panoramic image of the front part of the study area. mfA, massive fine ash; ALmCs, ash to lapilli massive clast supported; LmCs, lapilli massive clast supported; LBmCs, lapilli to block massive clast supported; mcA, massive coarse ash; ALmMs, ash to lapilli matrix supported; U, undefined lithology.

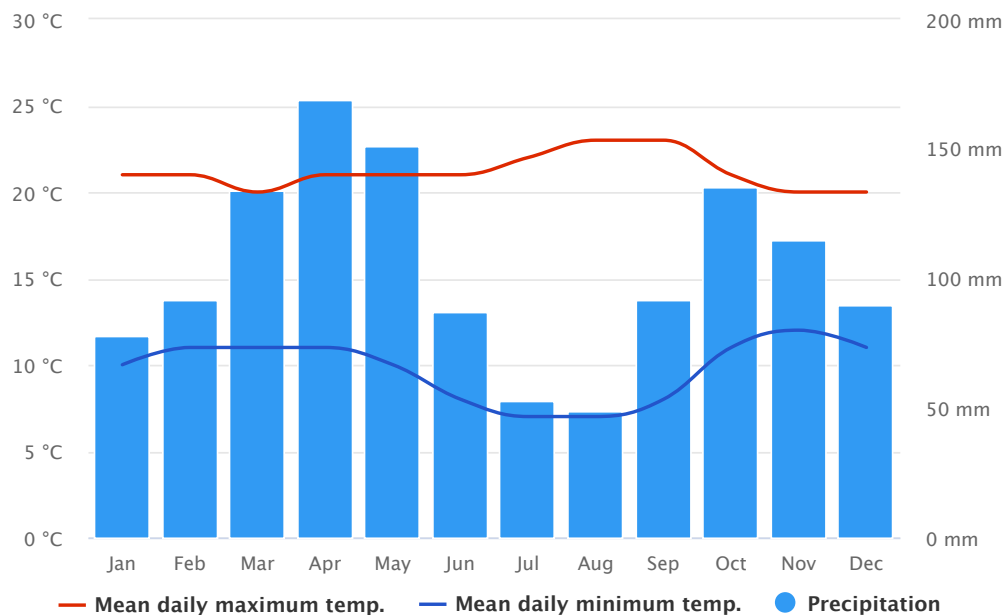


Figure 4. Weather archive of Urcuquí for 30 years. The histogram shows the return periods of maximum daily precipitation in the months of March, April, May, and October. The blue and red lines represent temperature ranges between 7° C and 23° C. Data obtained from Meteoblue®.

The current patterns of population distribution in the canton, make up a concentrated area that corresponds to the city of Urcuquí and its area of influence that involves a part of San Blas in such a way that they present the conditions to form a conurbation in the future. In the Urcuquí city there is a population of 15.671 people (INEC, 2010). Three-thirds of the population lives in poverty, while a quarter of this population lives in extreme poverty according to the Unsatisfied Basic Needs (UBN) method.

Table 1: Socioeconomic standing of Urcuquí population. Source: INEC 2010 National Population Census, based on UBN method.

Socioeconomic condition	Number of persons	Percentage (%)
Poverty	11361	72.50
Extreme poverty	5924	37.80

In Urcuquí city there are 4074 occupied private homes, of these 1035 homes are in acceptable habitability condition, 1.655 homes in a recoverable habitability condition and 1.374 homes in an irrecoverable habitability condition. Furthermore, 53.27% of households live in houses with inadequate physical characteristics, that is, 2.199 households and 863 households live in

overcrowded conditions. Thus, showing a qualitative housing deficit of 40.78% while the quantitative housing deficit is 33.73%.

An urban growth trend of Urcuquí city for the year 2030 (Fig. 5) was carried out through a multitemporal analysis using images from the LANDSAT and TERRA-ASTER satellites corresponding to the years 1986, 1991, 2005, 2007, 2009, 2012 and 2011. Most of the infrastructural development within the canton is moving concentrically towards the steep slopes that surround the city, due to the high price of the land in the central and more flatter parts of the urban area. One of these sectors is El Rosario, which as the other sectors close to the steep slopes are the most prone to natural hazards, including slope instability.

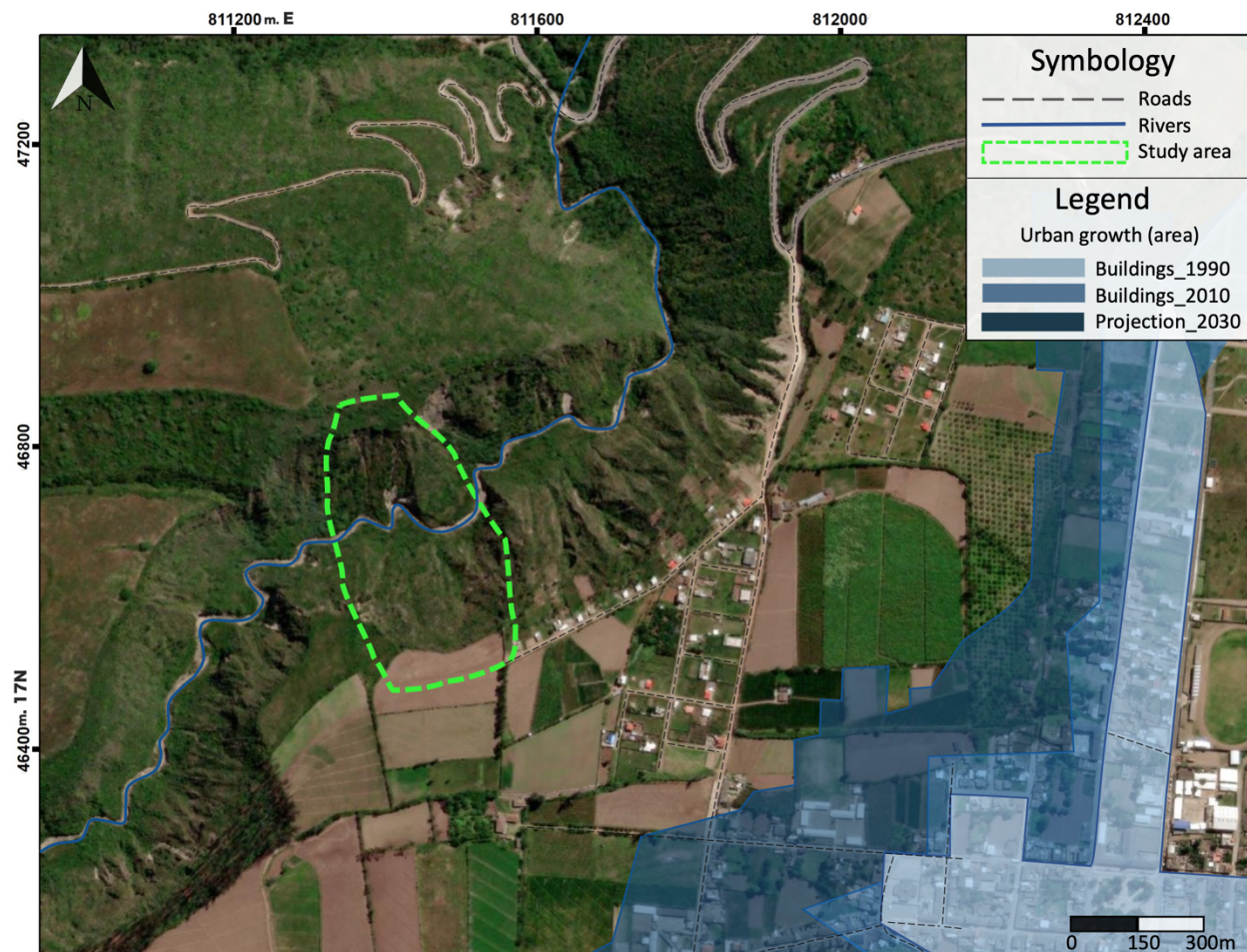


Figure 5. Urcuquí urbanization trend. Data obtained from GADMU.

Our study area, El Rosario, is outside the Urcuquí urban growth projection for 2030. However, in the recent years some infrastructures, in the majority houses, have already been built on the edge

of the Pinchinguela ravine, northwest of Urcuquí. The study area comprises a recently subdivided land, where the city has designed to build houses proximate to the slope instability area. The study case is even more problematic because in the top part of the ravine a material filling was done to flatten the area. These materials come from construction waste of Yachay Tech University, and the residents constantly dumping garbage and waste to filling the area. Figure 6 shows aerial images of the study area taken with a drone.

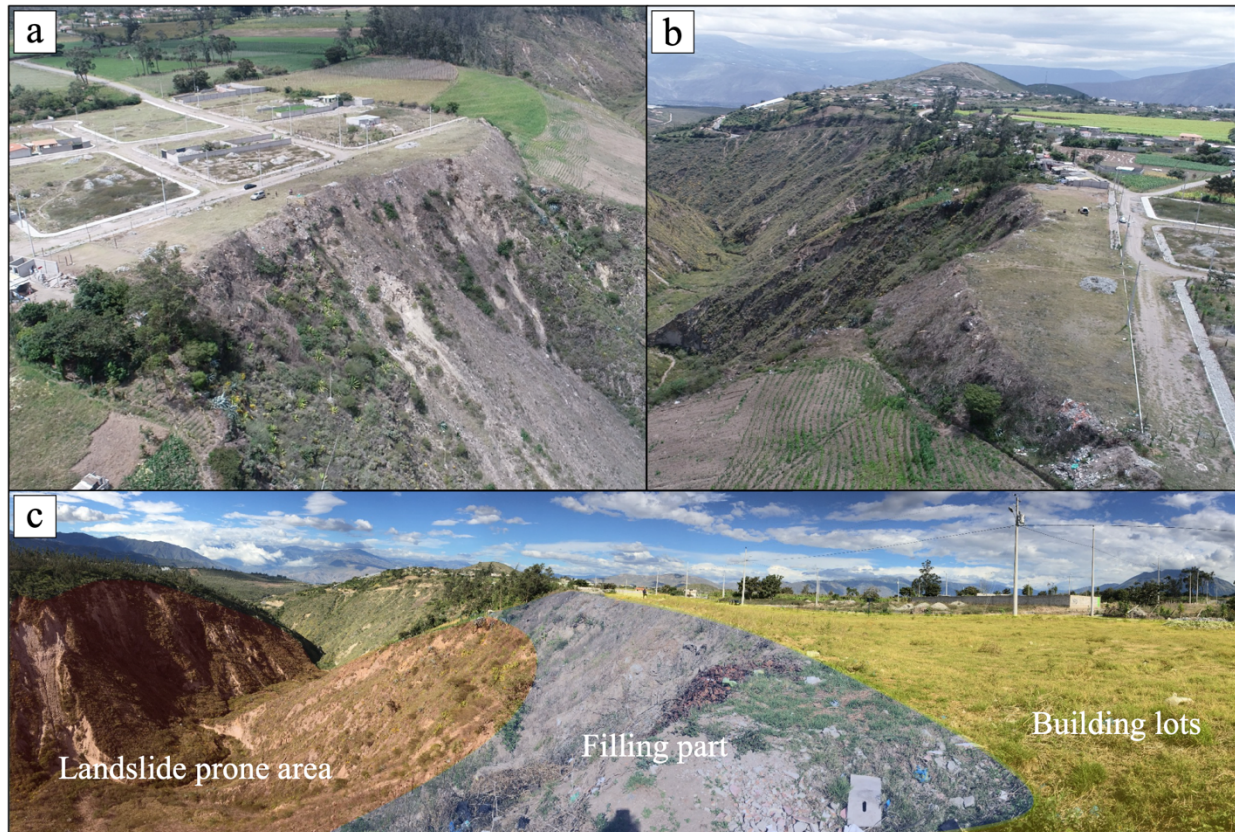


Figure 6. Panoramic images of the study area: (a) Right lateral view of the study area. (b) Left lateral view of the study area. (c) Panoramic view of the study area highlighting the slope instability-prone area (Red), the filling part (Blue), and the building lots (Yellow).

Based on this background, the area of research was adopted for the following reasons: (i) its steep slope, (ii) lithology; primary volcanic deposits denominated as poorly cohesive soils, (iii) an important contribution of water in the wet season, and (iv) anthropogenic activities; dumping of fill material or waste on the ravine. Also, it is necessary to mention that the study area has already been suffering some slope failure and landslides in the past.

METHODS

In the present research, UAV photogrammetry combined with SfM techniques has been applied to characterize a critical area of slope instability in the Pinchinguela ravine. The methodology employed in this work is described in Figure 7. The Phase 1 comprises a literature review of the study area, some information regarding this phase is described in the previous section Study Area. The Phase 2 starts the Data Acquisition stage of the work, which is divided into two main parts: UAV photogrammetry and Traditional topography. Phase 3 describes the workflow of these two methods and will be detailed below. Phase 4, Data Processing, utilizes data from both of these data acquisition methods, and has several steps explained in more detail in the Post-processing subsection of the Methods chapter. Finally, the Phase 5 will be described on the Results and Discussion sections of the present study.

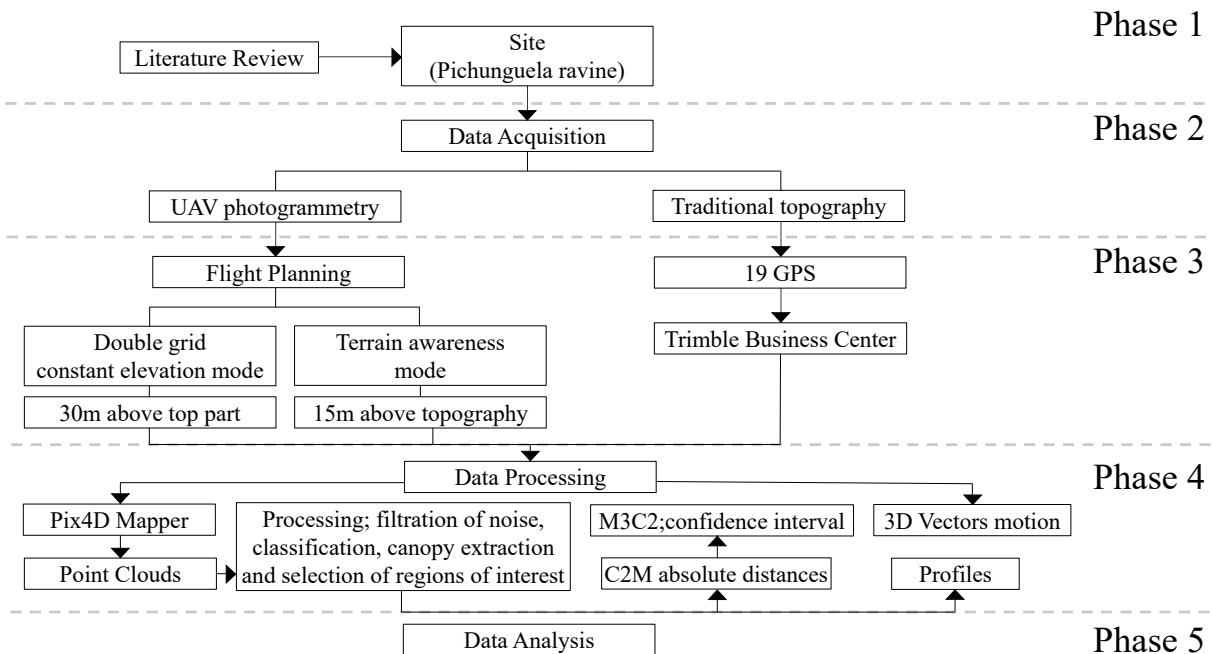


Figure 7. Workflow diagram of the study methodology.

UAV Photogrammetry

We performed monthly aerial photogrammetry campaigns from October 2020 to March 2021 over an area of approximately 0,171 km², covering the area of slope instability and the adjacent stable areas (Fig. 2). Two different flights plans were needed to cover the more interesting sections of the study area. DJI Inspire 2 drone equipped with a Zenmuse X4S camera was the

UAV equipment used for the aerial photogrammetry campaigns. The drone has a GPS system for positioning rectification which allows to record 3D coordinates (X, Y, Z) and attitude of the camera (roll, pitch and yaw) at every image captured (Shenzhen DJI Sciences and Technologies Ltd, 2021). Before each campaign, a calibration of the Inertial Measurement Unit (IMU) and compass was carried out to minimize the dome effect, which is explained in the following sections.

The accuracy of the photogrammetric measurement is mostly determined by the flying altitude and overlapping of the acquired images (Brückl et al., 2006; Kameyama & Sugiura, 2021). To be able to control this easily, Double Grid Constant Elevation and Terrain awareness flight plan modes were performed using Pix4D Capture and Drone Harmony flight planning software, respectively.

- ***Double Grid Constant Elevation Capturing Mode***

The Double grid flight plan at a constant elevation mode was implemented, covering a two-way path, N-S and W-E on the same flight plan. The specific settings on the Pix4D Capture software are the following: 70% image overlap, 90° camera angle, 250 m² area covered, and 30 m altitude. The flight altitude of 30 m is relative to the stable surface, which in this case corresponds to the road in the top part of the study area. This flight plan mode was implemented from October 1st of 2020, repeating the campaign approximately every month. A total of six campaigns were achieved using this mode of flight plan.

- ***Terrain Awareness Capturing Mode***

Despite the high overlapping provided by the double grid flight plan, the resolution of aerial photogrammetric data is also determined by the flight height (Brückl et al., 2006). Drone Harmony software presents a flight mode called Terrain awareness. This flight mode allows carrying out flight plan missions that consider the terrain's topography, i.e., obtain photographs at a constant distance between the drone and the ground. The specific settings on Drone Harmony software are the following: 80% image overlap, 90° camera angle, 100 m² area covered, and 15 m altitude. This flight plan mode was implemented from October

18th of 2020, but by the difficulty of access to the take-off area, only three flights were developed with this modality.

The application of aerial photogrammetry techniques always presents errors in the data acquired. One of the most common error is the so-called dome effect, which can alter the data significantly unless it is corrected. This effect is caused by the parallel alignment of the axes during image acquisition, the degree of overlap of the images, the absence of control points, or the incorrect estimation of the lens distortion parameters. Therefore, the effect is reduced by using accurate camera models, oblique and convergent images, and control points (Delgado, 2016).

Traditional Topography

Traditional topographic surveys were carried out on the same day as of the aerial photogrammetry campaigns from January 2021, measuring angles and distances of 19 ground control points. To record the topography data, reflective foil targets were set on each GCP (Figure 8.c). The planimetric and altimetric positions of the GCPs were scanned using Direct Refraction mode (DR) with a nominal accuracy of about ± 2 mm Trimble Total Station S5 (Trimble Geospatial, n.d.).

- ***Ground Control Points***

A total of 25 ground control points were strategically positioned over the two sides of the ravine. The network consists of 6 power electrical poles located on the road, 6 plastic cones located on the front part and 13 plastic cones located on side closer to the development area (Figure 8.a). The visibility between the instrument and the position of the GCPs was thoroughly analyzed, due to the terrain morphology (undulating topography, steps, ripples, etc. In addition, the surface is often covered with vegetation and there are also trees. Furthermore, the Total station equipment was set up in two points, on the stable side facing of the slope (Figure 8.a). Although the surveying scheme is not optimal because of the closeness of the two fixed points, the choice was made based upon on their visibility and upon the stability of the locations.

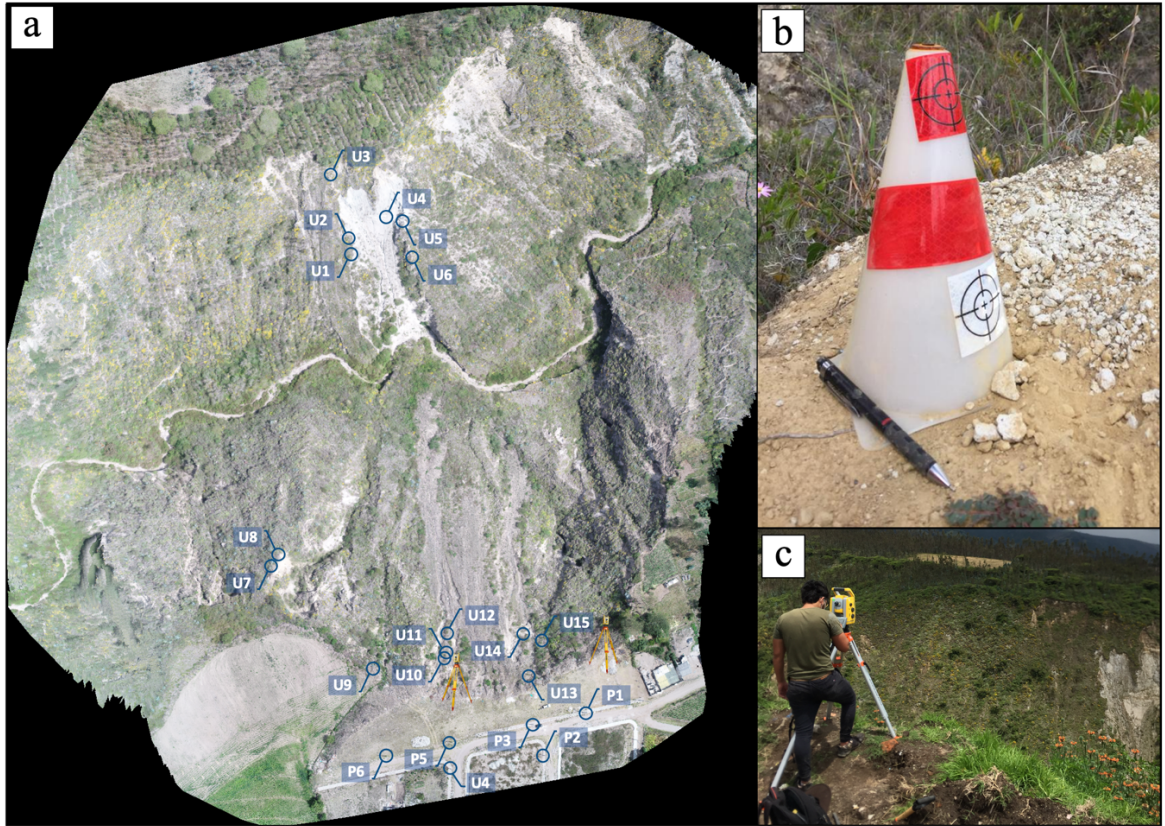


Figure 8. GCPs distribution and Total Station locations: (a) The network of GCPs, composed of 6 power electrical poles (P1-P6) and 15 plastic cones (U1-U15). (b) An example of the GCP with reflective targets 5 x 5cm. (c) The cone and stakes dimensions using with respect to the degree of consolidation of the soil.

The data obtained from these surveys were measured without a coordinate system. Trimble Business Center software was used to convert the X, Y and Z coordinates of each point in WGS84/UTM zone 17 N, EGM 96 Geoid. Then, the GCPs data were used in the Pix4D Mapper post-processing.

Data Processing

The processing of the images collected during UAV photogrammetry surveys were executed with the Structure from Motion based photogrammetry software Pix4D Mapper®. This SfM software can generate geospatial data such as DSMs, DTMs, orthomosaics and 3D dense point clouds readable by any other professional GIS package.

The process setting was carried out inside the Processing options section. Considering the complex terrain in which the study was developed, advanced settings were necessary for accurate reconstruction. This section is divided into three subsections:

Processing 1: *Initial Processing*

This step automatically extracts the key points from the images to calculate the true camera location and some orientation parameters of the images using Automatic Aerial Triangulation (AAT) and Bundle Block Adjustment (BBA). In this step, a sparse point cloud is generated in addition to a preliminary quality report of the process.

Once this step is finished, we load the corresponding 3D data of 25 GCPs to align the model to our coordinate system WGS84/UTM zone 17 N. Also 10 check point (CPs) were selected manually in at least three separate images for each data set. This option allows to reoptimize the reconstruction using the data from traditional topography (Agüera et al., 2017).

Processing 2: *Point Cloud and Mesh*

In this step, we only focus on the generation of a Densified Point Cloud, which is the base data for the rest of the study.

Processing 3: *DSM, Orthomosaic and Index*

Finally, the third step of the processing allows generating a DEM and an Orthomosaic. It is also possible to obtain a global processing Quality Report, which has the information regarding to the Root Mean Square errors (RMS). An example of the Quality Report from the post-processing images is shown in Appendix 1.

The time required to complete this process is determined on the quality level selected and the processing power of the PC. In this study we worked with an Intel (R) Core (TM), CPU i7-7700 @ 3.60GHz, 8.0 GB of RAM, Windows 10 Pro, 64 bits, graphics card Radeon RX550/550 Series (Driver 27.20.1034.6).

- ***Processing of point cloud raw data***

The purpose of processing of point cloud raw data involves the filtration of noise, classification, canopy extraction and selection process of the regions of interest. The classification of point clouds was developed following the instructions and parameters established in previous studies (Brodu & Lague, 2012), using the Train Classifier tool of the CANUPO plugin on Cloud Compare software. Most of the surface is covered by vegetation, mainly by grass and shrubs. Hence, the vegetation layer does not allow the faithful reconstruction of real shape of the ground. We used the Classify tool of the CANUPO plugin on Cloud Compare software to remove the points with values corresponding to vegetation and noise. The use of CANUPO plugin, which has a classification rate of about 98%, enables direct comparison of the surfaces (Brodu & Lague, 2012).

Finally, to account for the relative accuracy of aligning and scaling of the points clouds, the Iterative Closest Point (ICP) algorithm was used for a final check-up that any systematic misalignment between the point clouds does not influence the comparison process (N. Ahmad et al., 2018). Despite the point clouds already being in the same coordinate system; this process improves the alignment through very small values of translations and rotations. To reduce the time for processing the last step was to select of the certain regions of interest.

Spatial Analysis

Once the point clouds are processed, the analysis consists of looking at the existing differences between them. The differences are related to displacements and changes of the morphology of the terrain. For this spatial analysis we used both Cloud Compare and AutoCAD Civil 3D software.

Cloud Compare is a three-dimensional point cloud processing and editing open-source software. This software is designed to calculate changes on simultaneous point clouds, which are mainly derived from SfM techniques. It integrates not only direct comparison tools but also

algorithms for registration, resampling, scalar field management, calculation statistics, and better visualization tools. Regions of instability (loss of volume) and deposition (increase in volume) can be depicted in three dimensions.

The complex interaction between removal and deposition occurring simultaneously in the area make it difficult to measure and quantify specific zones of failure. AutoCAD Civil 3D allows to obtain accurate transversal profiles with the respective relevant information of the planimetric and altimetric displacements on two specific segments of the most critical areas of the two sides of the ravine.

- ***Three-dimensional Comparison***

To identify and calculate potentially instable areas require the comparison of at least two point clouds (Lague et al., 2013). Two types of distance calculation are available on Cloud Compare: Cloud to Mesh distances (C2M), which estimates distances between a point cloud and a mesh and Multiscale Model to Model Cloud (M3C2), which calculates distances between two-point clouds along a cylinder of a given radius projected along the normal surface direction. The point cloud corresponding to October 1st of 2020, was denominated as the reference cloud, and the other ones as the compared clouds.

Cloud to Mesh Comparison: *C2M*

The direct method calculates distances between the reference cloud (local normal of the mesh) and the compared cloud datasets (Fig. 9). It was developed for rapid change detection on point clouds rather than measuring distances accurately (Girardeau-Montaut et al., 2005).

First, a mesh must be created from the reference point cloud (October 2020). The mesh results from the Poisson Surface Reconstruction method, where the point cloud is projected in 2D and all the points are correspondingly triangulated, and then the resulting mesh structure is reconstructed to the original point cloud (Kazhdan et al., 2006).

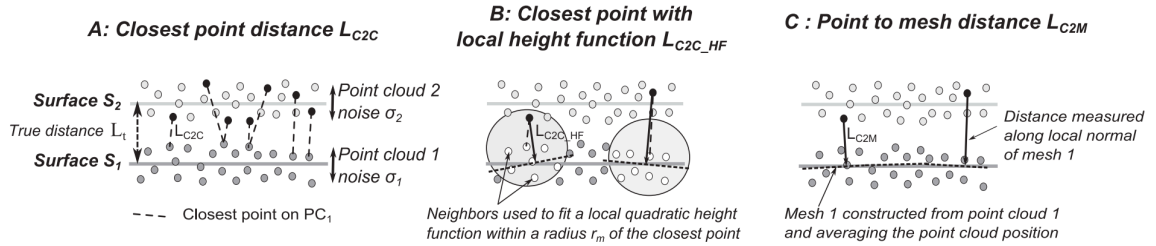


Figure 9. Illustration of the difference between both Cloud-to-Cloud distance (C2C) and Cloud to Mesh distance (C2M). Where each point cloud has a roughness parameter (σ) related to the noise and surface roughness. A: Closest point distance; the distance between the closest points of the reference cloud and the compared cloud. B: Closest point distance with local height function; the distance between the point cloud 1 to the point cloud 2 at a defined radius. C: Point to mesh distance; the distance between the local normal of the mesh (reference point cloud) to the corresponding closest point on the point cloud 2 (Lague et al., 2013).

C2M distance estimation is greatly influenced by the quality of the mesh. The mesh generated by the Poisson Surface Reconstruction method interpolates the gaps and missing data due to for example vegetation extraction, resulting in erroneous surface reconstruction in some areas.

Multiscale Model to Model Cloud Comparison: *M3C2*

The *M3C2* plugin proposed by Lague et al (2013), is specially designed to accurately detect small changes in complex terrains with rough and variable surfaces. The *M3C2* comparison method has three characteristics: (i) It operates directly on point clouds without meshing or gridding. (ii) Computes the local distance between two-point clouds, in a direction normal to the surface, which detects variations in orientation. (iii) Allow to estimate a confidence interval for each measure depending on point clouds roughness and registration error on a common coordinate system (Lague et al., 2013). The process to compare the two-point clouds using *M3C2* plugin is carried out in two steps:

The first step is calculation of the normal vector N for each point or core point (sub-sample version of the original point cloud; to reduce process), by fitting a plane to the neighboring points that are within a radius of $D/2$ (Fig. 10). The parameter D is the normal scale, and

it is defined by the user taken into consideration the local roughness of the point cloud (Lague et al., 2013).

The second step is the measurement of the estimated mean distance between i_1 and i_2 . That mean value corresponds to the average positions of the points found in each point cloud (n_1 and n_2), within a cylinder along the collinear axis of the normal vector obtained from the previous step. The diameter of this cylinder is the parameter denominated as projection scale (d), and the length of the cylinder is the parameter denominated as maximum depth. The standard deviation of the distance distribution in each point cloud, gives a local estimate of the point clouds roughness $\sigma_1(d)$ and $\sigma_2(d)$, useful parameter to define the local accuracy of the distance measurement.

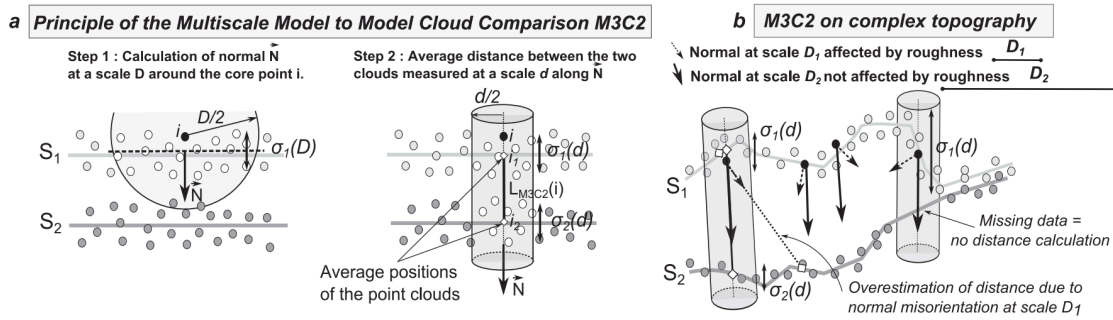


Figure 10. Illustration of the two steps of the M3C2 comparison process(a) and the function on complex topography(b) (Lague, 2013).

In complex rough surfaces, a given value similar to the local roughness at the normal scale (D_1) will detect an incorrect normal direction and consequently overestimate the distance between the two-point clouds; a larger scale (D_2) will be able to compute a more uniform normal orientation, reducing the influence of the local irregularities (roughness). However, the normal scale should not be too large either because it increases the standard deviation $\sigma(d)$, which increases the confidence interval and thus will not give as accurate distance estimation.

When there is an absence of corresponding points in the compared clouds, the M3C2 algorithm does not make an interpolation, and it just does not compute any difference. It

may be by missing data in that area or that the points of the other cloud are further away than the maximum height that we have set, which is why the program interprets that there are no equivalent points.

A comparison between different D values, using a preferred orientation on +Z, oriented with the Minimum Spanning Tree method, was carried out until finding an optimal value of the normal scale for our case study. We did the distance calculation to the whole point cloud to test how well the M3C2 works through looking at the unchanged regions of the survey area.

Considering the previous C2M distance results, the planimetric and altimetric differences found on the profiles (shown later), the average roughness of the point cloud equal to 0.26 m, a D of 2 m were defined. The last step of this process is to estimate the confidence interval. This is crucial since we want to know what is the statistically minimum change that is larger than the errors related to the alignment and roughness of the point clouds. This confidence interval can be estimated through confidence level at 95 % level of detection ($LOD_{95\%}$) given by the registration error, *reg*. (Equation 1).

$$reg = \sqrt{(RMSE_{Ref.point\ cloud})^2 + (RMSE_{Comp.point\ cloud})^2} \quad (1)$$

Level of Detection at 95% (Equation 2).

$$LOD_{95\%} = \pm 1.96 \left(\sqrt{\frac{\sigma_1(d)^2}{n_1} + \frac{\sigma_2(d)^2}{n_2}} + reg \right) \quad (2)$$

where:

- *d* is the projection scale.
- $\sigma_1(d)^2$ and $\sigma_2(d)^2$ are the average local roughness of the point clouds along the normal direction.
- n_1 and n_2 , are the average numbers of point found within the cylinder
- *reg* is the registration error Eq. (1)

3D Vectors Motions

GCPs data obtained from traditional topography can also be used to provide displacement or deformation rate information of specific regions of the slope, where the GCPs are located. To obtain information on the displacements of the GCPs, a Point Comparison report was generated in Trimble Business Center software, which takes into consideration the following parameters: horizontal/vertical range (0.20 m) and horizontal/vertical tolerance (0.5 m), providing information of the horizontal, east, north, and vertical deviation of pairs of points (See Appendix 2). In addition, polylines from each set of GCPs coordinates were created, using the AutoCAD Civil software.

- ***Two-dimensional comparison***

Finally, an effective way to compare the ground deformation at different times are the profiles extracted from the post-processing point clouds. The profiles were generated using AutoCAD® Civil 3D 2021, where the process consists of creating a surface from the point cloud, drawing the lines of the corresponding interest areas, creating the profile by means of a lineation, and finally displaying the abscissas and elevation information corresponding to the profile. Planimetric and altimetric displacements can be obtained as a product of the volumetric changes through two different profiles of each cloud point (October, December, and March).

RESULTS

The first UAV-SfM derived products resulting from the post processing are the orthophotos of the area in correspondence of each survey (Fig. 11).

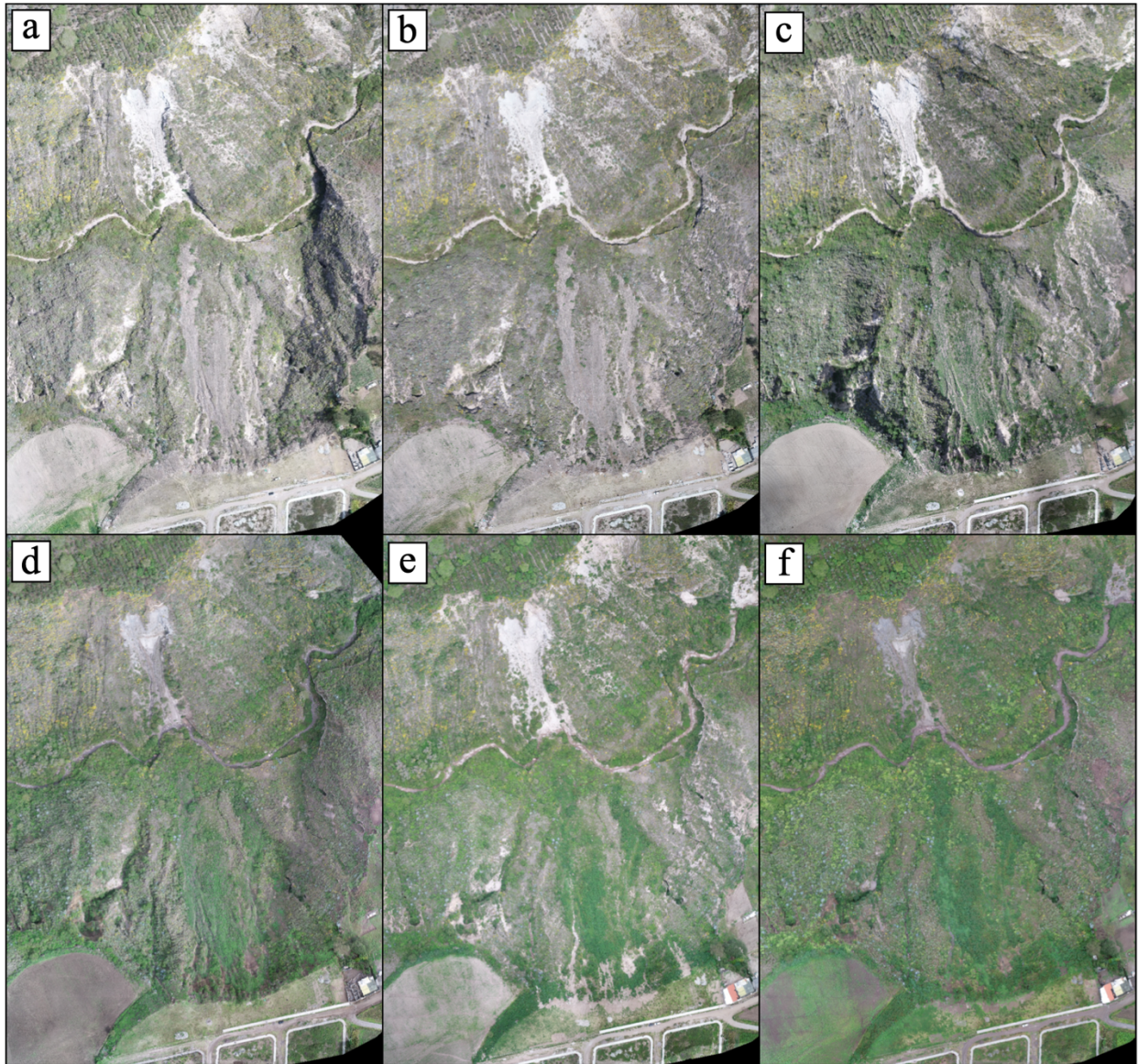


Figure 11. Orthophotos obtained from the UAV-SfM process using the Double Grid flight plan. a. October 1st 2020, b. November 1st 2020, c. December 20th 2020, d. January 1st 2021, e. February 06th 2021, f. March 1st 2021.

An average area of around of 0.158 km² was covered in each campaign corresponding to the Double Grid flight plan. The ground sample distance (GSD) which is the parameter correlated to

the resolution of the results obtained is between 4.04 to 3.97 cm/pixel. It means that the minimum feature represented in the Orthomosaic has a dimension of 4 cm. Regarding the results of the campaigns using the Terrain Awareness flight plan mode, the results are different. The campaigns of January 18 and February 21 covered an area of around 0.005 km² and reached a resolution of 0.56 and 0.63 cm/pixel, respectively.

Table 2: Average GSD obtained from UAV-SfM process and the respectively area cover for each campaign.

Date	GSD (cm/pixel)	Area covered (km²)
01-Oct	4.03	0.158
01-Nov	4.04	0.171
20-Dec	3.97	0.157
01-Jan	3.98	0.149
18-Jan	0.56	0.006
06-Feb	4.01	0.161
21-Feb	0.63	0.005
02-Mar	4.01	0.157

The differences in the results are directly associated with the following parameters corresponding to the post-processing on Pix4D Mapper software: First, the number of images obtained in each campaign is not the same, and there is a difference of up to 31 photos between them. However, this parameter does not influence the number of key points per image, which is defined by the image size (difference in flight height) and shows the number of points that can be detected per image. The camera optimization parameter is the relative difference between initial and optimized internal focal length. The optimal percentage is less than 0.5%, but numbers near this range are also valid allowing a good optimization process. The number of matches that have been calibrated per image is around ¼ of the key points per image. Finally, the georeferencing parameters show that 3D GCPs were used to align the model to an established coordinate system (Table 3).

Root Mean Square Error (RMSE) is the parameter that allows us to evaluate the quality of the georeferencing of the obtained products. This parameter measures the distance in meters of change per pixel due to the processing. The RMSE_{X,Y,Z} corresponding to the processing of UAV images are presented in Table 4.

Table 3: Information related to the UAV campaigns and processing on Pix4D Mapper.

Date	Keypoints per image	Dataset (Images calibrated)	Camera optimization (%)	Matches per calibrated image	Georeferencing
01-Oct	86406	553/553	0.63	24887.6	Yes, 3D GCP
01-Nov	76198	557/557	0.74	23188.7	Yes, 3D GCP
20-Dec	85743	580/580	0.66	27530.1	Yes, 3D GCP
01-Jan	86464	549/549	0.72	25130.5	Yes, 3D GCP
18-Jan	72726	118/200	0.63	4547.7	Yes, 3D GCP
06-Feb	71867	562/562	0.54	24335.0	Yes, 3D GCP
21-Feb	72598	121/204	0.51	5627.9	Yes, 3D GCP
02-Mar	95602	562/562	0.84	29697.8	Yes, 3D GCP

All the models revealed acceptable accuracies in the georeferencing alignment. However, a notable difference between RMSE values of the three first campaigns to the last ones is the number of control points used. In the first ones (October, November, and December), only 6 GCPs corresponding to the power electrical poles of the area were used, and in the last ones (December, February, and March), the whole network of 25 GCPs were implemented.

Table 4: Absolute geolocation variation. RMSE [m].

Date	RMSE_x	RMSE_y	RMSE_z
01-Oct	1.765309	1.911744	1.446740
01-Nov	1.768591	1.912509	2.819606
20-Dec	1.946044	2.123549	1.766322
01-Jan	0.218119	0.221781	0.160448
18-Jan	0.555510	0.339869	0.613330
06-Feb	0.215746	0.349759	0.222904
21-Feb	0.474041	0.774968	0.336356
02-Mar	0.186070	0.182326	0.174668

Another of the results obtained with the processing of the UAV images in Pix4D Mapper software are the dense point clouds of the area, which are georeferenced to the local WGS84/UTM zone 17 N. The surface information in point cloud data consists of millions of points, with each point defined by X, Y, and Z coordinates. Also, each point is associated with the RGB color and classification value, which defines the type of element it represents (vegetation, soil, buildings,

etc.). Its models are more accurate in reconstructing the spatial relationship of topographic features and structures than the Digital Elevation Model (DEM) or Digital Terrain Model (DTM).

Dense point clouds generated from UAV-SfM techniques create surface outliers or noise. Furthermore, points that have values of vegetation, building, and any non-surface values were removed with 98% certainty using the CANUPO plugin available on Cloud compare software. Also, as mentioned in the methods section, the ICP alignment was carried out to improve the alignment of point clouds to a reference cloud (October 2020).

Table 5: Final RMSE values corresponding to the ICP alignment on Cloud Compare software.

Date	RMS_x	RMS_y	RMS_z	Final RMSE [m]
01-Oct	1.765309	1.911744	1.446740	0.018510
01-Nov	1.768591	1.912509	2.819606	0.019722
20-Dec	1.946044	2.123549	1.766322	0.018016
01-Jan	0.218119	0.221781	0.160448	0.012611
18-Jan	0.555510	0.339869	0.613330	0.013825
06-Feb	0.215746	0.349759	0.222904	0.015901
21-Feb	0.474041	0.774968	0.336356	0.011937
02-Mar	0.186070	0.182326	0.174668	0.011679

The point clouds that resulted from the ICP alignment was used for the distance comparison analysis on Cloud Compare.

Cloud to Mesh Comparison results

The results of distances between the point clouds and a referenced three-dimensional mesh (October 2020) have been calculated and added to each compared point cloud. The corresponding distances that define the surface changes can be visualized with a scalar field, where red colors indicate positive distances and blue negative distances. Furthermore, negative distances mean that the reference mesh is under the point cloud compared, which allows to interpret areas of removal of material, whereas on the contrary, the positive distances could be interpreted as areas of deposition of material. Also, points without any corresponding value in the compared point cloud remain in color gray.

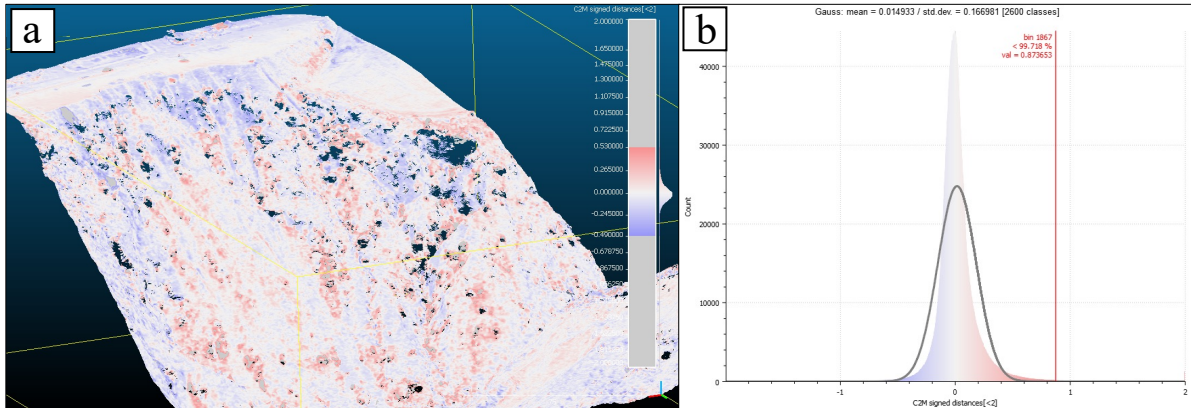


Figure 12. Cloud to mesh distance values in meters between October 2020 to December 2020. (b) Gaussian plot represent the distribution of the C2M absolute distances between the two point clouds, mean and standard deviation are also indicated.

The Gaussian plot in Figure 12.b, aids in the visualization and interpretation of the data obtained from C2M process. Its vertical axis indicates the number of detected points, while its horizontal axis indicates the absolute distance between the reference point cloud(mesh) to the compared point cloud. Most observed points fall within a range of - 0.49 to 0.53 m (three standard deviation; 99% of the points), followed by a small group of points that reaches up to 0.90 m. The red peak at the tail of the plot could be related to a zone of points that appears only in one of the clouds, where the distance is overestimated. It generally occurs because of missing data, gaps, and at the edges of the models.

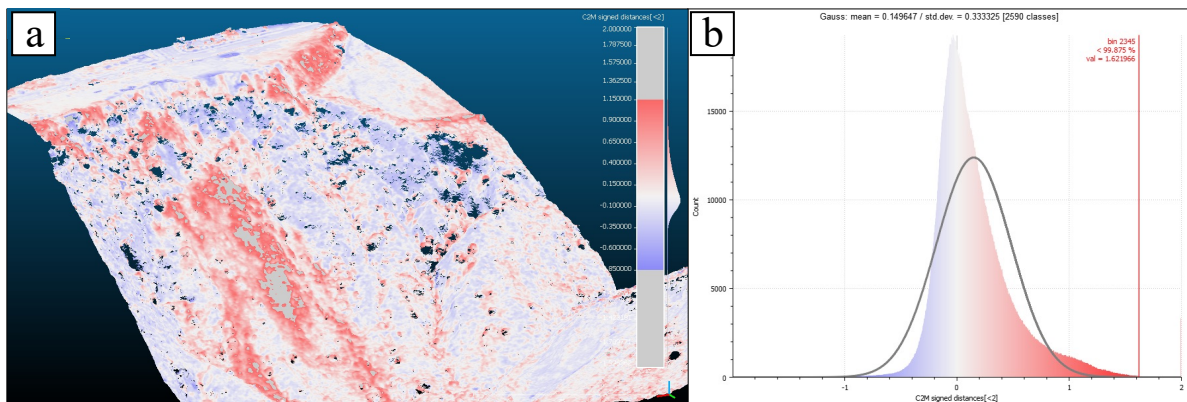


Figure 13. Cloud to mesh distance values in meters between October 2020 to March 2021. (b) Gaussian represent the C2M absolute distances between the two point clouds, mean and standard deviation are also indicated.

In the same way, the Gaussian plot that correspond to the C2M results between October 2020 to March 2021 shows that almost all the points fall within the range of -0.85 to 1.15 m, followed by another small group of positive points that reaches up to 1.62 m. Also, the red peak at the tail of the histogram could be related to a zone of points that appears only in one of the clouds. However, it could be related to large displacements not calculated by the algorithm.

The C2M comparison of both surveys reveals that the study area experience significant movement in the period of study. The accuracy of the absolute values obtained are restricted by the interpolation of data from the reconstruction of the mesh, where the process could smooth many details of the point cloud data. The distance values were used for a preliminary detection of the removal and deposition areas within the study area. Also, these results provide information to determine the normal scale to M3C2 comparison.

Multiscale Model to Model Cloud Comparison results

The M3C2 results using a normal scale equal to 2 m were attached to the compared point cloud. The information related to the M3C2 distance, distance uncertainty and significant change can be visualized on the program. The average roughness estimate at scale D was 0.026 , confirming that the normal scale of 2 m is suitable for this study, being more than 25 times greater than the average roughness. The RMSE of the reference point cloud is equal to 0.018 m, and the average RMSE of the compared point clouds is equal to 0.015 m. Using the equation (1) the average reg value is 0.024 .

The data acquired has been influenced by multiple errors. However, a confidence interval has been attached to each distance measurement, which help to tests the statistically significance LOD_{95} in the comparisons analyzed. The confidence interval is a factor of the cumulative effects of the errors related to the instrument measurement, roughness effects and point cloud alignment uncertainty. Therefore, even if the surface did not change, a small difference would be systematically measured in the wrong way. A correctly defined confidence interval should rule out the difference as not statistically significant. When a real change of the surface occurs between campaigns, the pattern of relative changes should be visible and repetitive in each of the results. Confidence level is calculated with the $LOD_{95\%}$ equation (2), resulting in an

average value equal to 0.098 m. Therefore, the relative morphology changes on some specific areas, which have been previously chosen as the most representative.

In the same way as with the C2M interpretation of the results, the negative values show areas of loss of material, and positives ones could be associated to material accumulation areas. The area highlighted with a green ellipse shows the most critical areas of remotion on the slope. Points without any corresponding point (NaN) in the compared point cloud remain in color gray, shows the points that could not be found on the other point cloud within the cylinder dimension of the normal scale. They are mainly associated due to the lack of data points or holes in the data sets, or simply implies that the maximum length of the cylinder is not long enough.

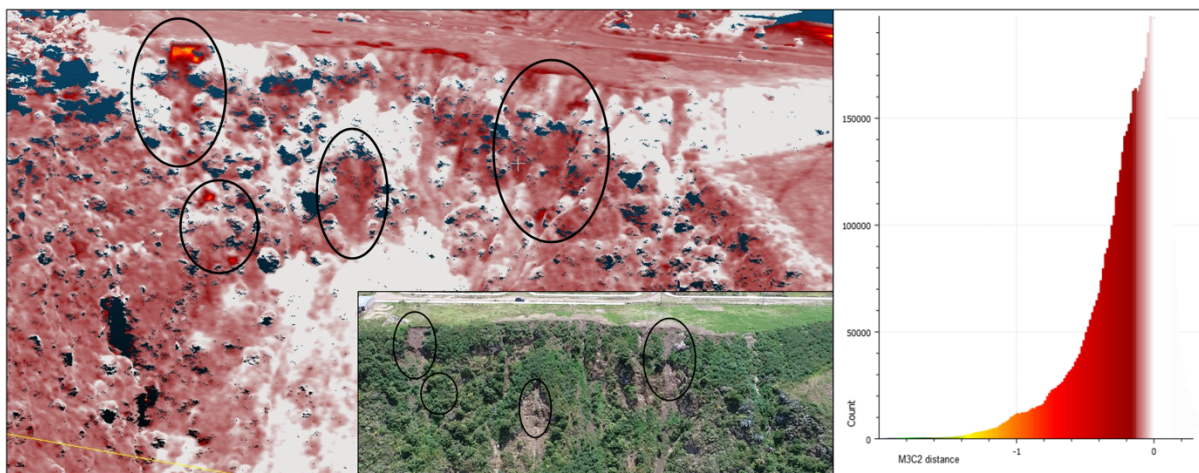


Figure 14. M3C2 distance calculation between the October 2020 to March 2021 surveys of the filling part with the respectively Gaussian plot; highlighting the most critical areas of remotion of material.

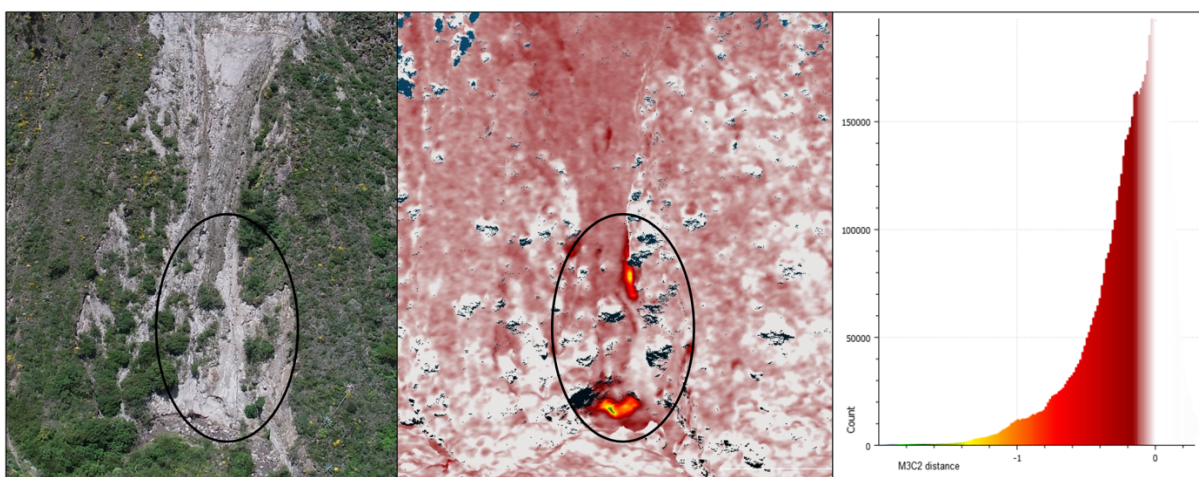


Figure 15. M3C2 distance calculation between the October 2020 to March 2021 surveys of the front part with the respectively Gaussian plot; highlighting the most critical areas of remotion of material.

The distance uncertainty values increase in areas where the calculations could not be carried out successfully. The distances uncertainty on stable regions is nearly close to zero, or around to 0.12 m. In the stable parts, the location of the car can be identified, showing a level of uncertainty valid, its position is a sporadic feature located on different positions on each campaign, and which were not removed to probe the validity of the process. Finally, the larger values of uncertainty show the non-stable areas, where the erosion, displacements and any detachment possibly were occurring during the time of study.

The significant change values correspond to real change detected by the setting imposed by the user. In our comparison most of the area is red, which means that the calculation are statistically significant. Furthermore, the saturation can be increased to highlights these areas. Within this context, the red areas means that there is uncertainty in those points. The closer to zero the values are the better.

The more visible displacements have been corroborated with aerial images taken with the drone after each double grid and terrain awareness UAV campaign. Negative values (removal of material) are commonly located in the steep areas at the top part of the slope, while the positive values (deposition of material) are localized at the foot of the two side of the slope.

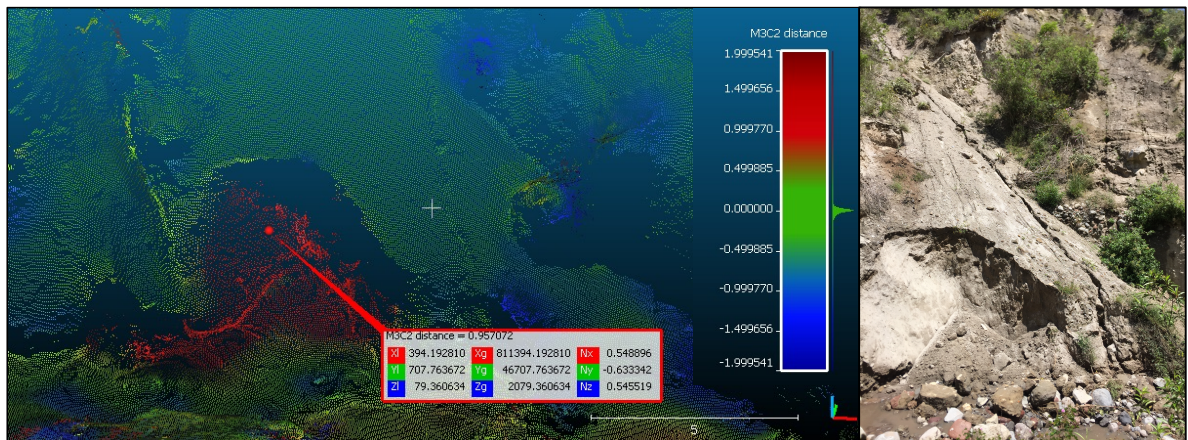


Figure 16. Critical areas of remotion within the front slope.

C2M and M3C2, provide information relating to movement of critical sections or region of the slope. The anomalous terrain displacement values obtained can be due to the errors on the

filtration and canopy extraction, which are representing changes on vegetation height. However, the 3D vector motions results from traditional topography coincide approximately with the dip direction of the slope.

These results allowed a first estimate of the magnitude of the ground movement but is not sufficient to describe the kinematics in the slope. These changes, termed as “mass balance” show that the material removed is deposited on the same slope. Therefore, the use of data from tradition topography could provide the necessary detail required for the subsequent analysis and interpretation of these morphological changes over time.

3D Vector motions

By means of Total Stations it's possible to detect movements on the order of mm/yr or cm/yr. For that, the GCPs data could be used to determine 3D motion vectors. In Figure 19 the vectors displacement corresponding to each plastic GCP can be visualized. In the right panel of the same image, the 2D projected vectors corresponding to the polylines created in AutoCAD civil 3D software show a display of the movements and displacements that those GCPs have experienced trough the 5 traditional topography surveys (each vertex represents a 3D coordinate for the respective survey). The polylines corresponding to the GCPs located on the front slope of the study area: U1, U2, U3, U4, U5 and U6 (Fig. 8). The polyline corresponding to the U4 GCP only has four vertexes since it is in the center of the more critical area of movement, causing large displacements until it was finally removed from its position. The same happened with other plastic GCPs that were not considered for the study because after one to two surveys they were completed removed from their position.

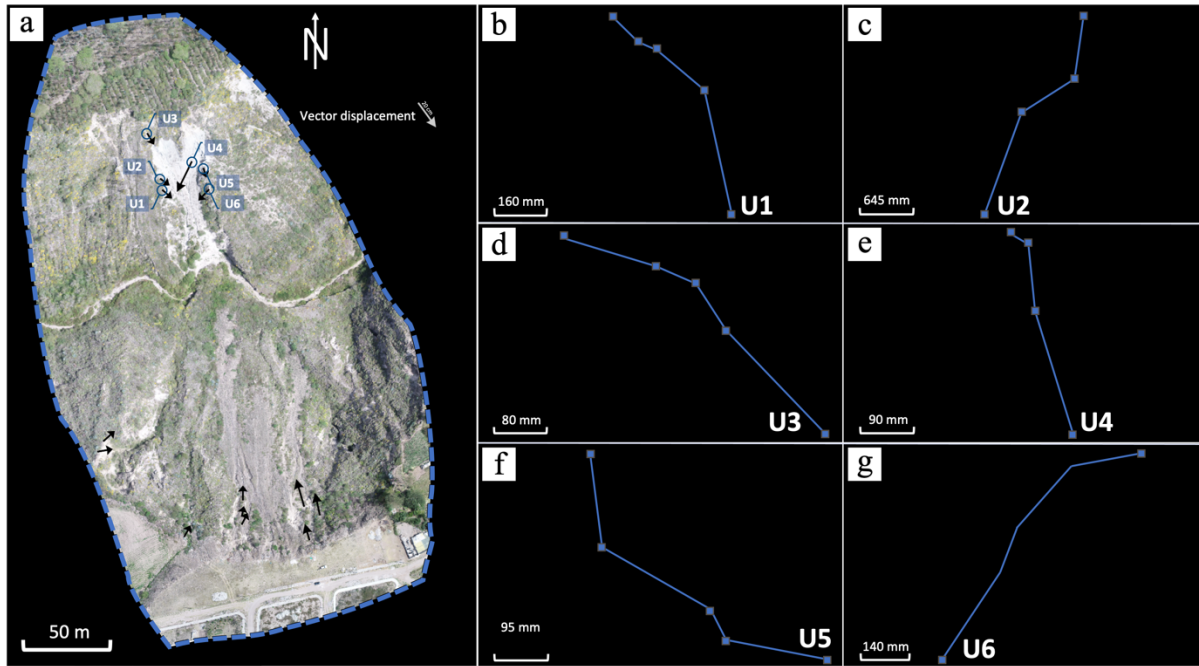


Figure 17. Displacement vectors from the GCPs data, derived from traditional topography surveys since December 2020 to March 2021(a), b. U1 GCP, c. U2 GCP, d. U3 GCP, e. U4 GCP, f. U5 GCP, g. U6 GCP.

The advantage of GCPs measurements from traditional topography in comparison to the others results derived from UAV-SfM process, is that it only presents the manufactured error of the instrument Trimble Total Station on the mode Direct Refraction. The final displacements results evidencing movements on the order 0.006 to 14.8 cm/month. The displacements observed coincide approximately with the dip direction of the slope.

Profiles

Two profiles were extracted from the point cloud datasets. The first one is located on the South part of the study area (Fig. 20). In the same figure a critical section highlights the difference in altitude between the profiles in correspondence of the same planimetric position. This profile start from the stable north side of the slope, crosses the slope, and rises the stream bottom part. Clear differences between the profile of October to March are visible, in the top part a remotion of material corresponding to 10 cm between October to December can be observed, following by a small increase from December to March, which is related to the debris cleaning works in the upper part. In the middle of the profile (at 2244 m of altitude) there is not a noticeable

difference between October and December. However, a material removal of up to 1.10 cm corresponding to the March surface is clearly visible in the profile comparison. Finally, following the same pattern at the bottom of the slope at 2225 m altitude, a subsidence of up to 93 cm is observed.

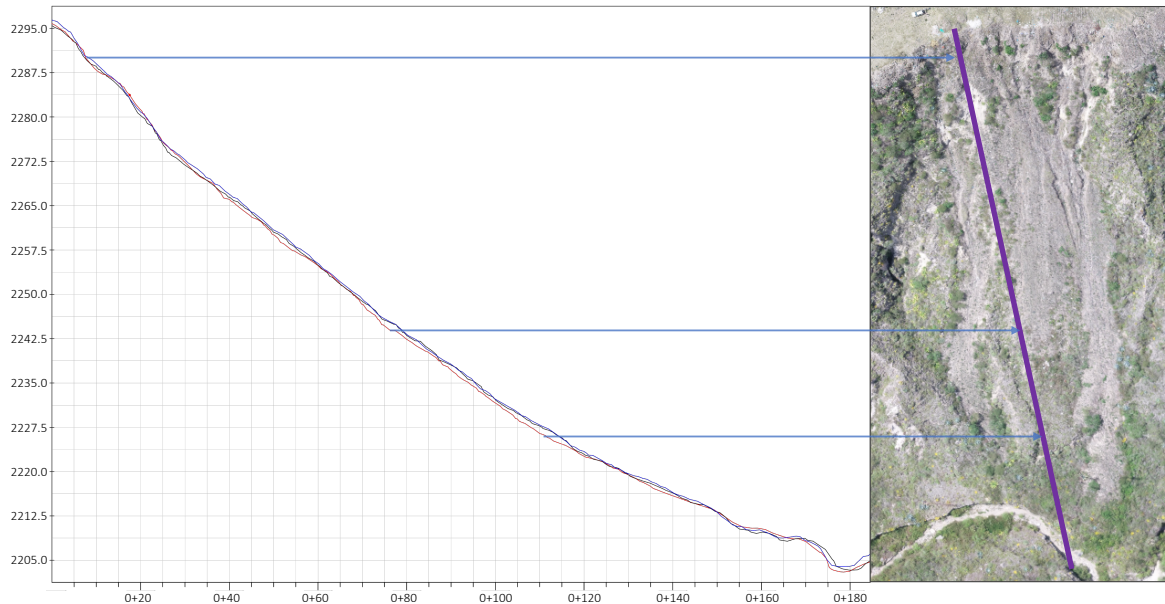


Figure 18. Profile along the North. Cross sections concerning October (Blue), December (Black), March (Red). A detail of the same section that highlight and quantifies the difference in altitude between the profiles

In Profile North, planimetric and altimetric displacements greater than the North profile have been observed. This may be related to the fact that this profile is located in the central axis of a pre-existing landslide, which can be influenced by the kinematics of the same. In the same way, this profile can provide accuracy information since the lack of vegetation makes the site more suitable. In the top part, above of 2880 m an interaction between removal and deposition of material is observed, at 2880 m a detachment of consolidated material could have caused that abrupt difference of 80 cm. In the middle of the profile at 2245 m, a linear interaction is observed, which is according to the topography of the area, despite that the profile corresponding to March is above that of December, the reason could be related to the dynamics of removal and deposition of material on the slope. Finally, at the bottom of the slope at 2223 m of altitude, the cracks that are formed by the action of the water, generate this topography in the form of a zigzag, according to the profile of the southern area, in this area the morphology corresponding to March is above of the rest, because of deposition process.

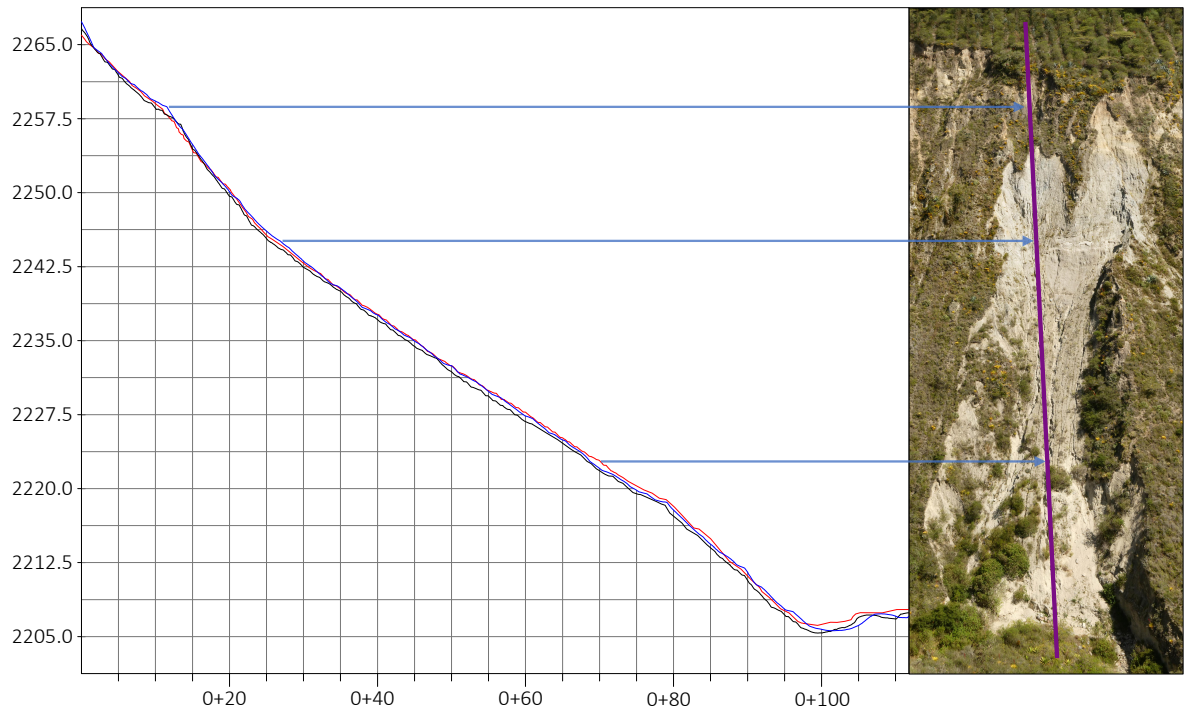


Figure 19. South profile. October (Blue), December (Black), March (Red).

The results of this last technique, which was corroborated with the previous results has revealed that the slope area has moved significantly over a period of ~6 months (October 2020 to March 2021).

DISCUSSION

UAV photogrammetry data processed with SfM software allows elucidating the morphological changes in the slope instability areas by obtaining derived products such as dense point clouds and orthophotos with high spatial, accurate and temporal resolution (Giuseppe Esposito et al., 2017; Preston, 2021; Rocca, 2020). UAV-based SfM is an applicable methodology to a wide variety of structural data needs (Peterson et al., 2015). Almost anything that can be photographed technically can be modeled and reconstructed (Nex & Remondino, 2014; Peterson et al., 2015).

The main advantages of UAV photogrammetry are the collection of data over large, dangerous, and inaccessible areas over a short period of time. It is transportable equipment that does not need to be installed on or near the potentially unstable portion of the slope, reducing health and safety risks (Agüera et al., 2017; Cao et al., 2019; Eker et al., 2018; Hugenholtz et al., 2015; Kameyama & Sugiura, 2021; Nex & Remondino, 2014). Despite the methodology's good performance, UAV-SfM derived products cannot completely replace the in-situ slope-monitoring techniques in situ such as extensometers, inclinometers, prisms, and radar systems (Barla et al. 2017; Atzeni et al. 2015).

Some difficulties in surveying the study area using UAV photogrammetry can be caused by the terrain topography, by slope gradient, by the presence of thick vegetation, and by how visible the study area is from the air (Z. A. Ahmad et al., 2017; Nieto Masot et al., 2016; Stöcker et al., 2015). Some of these problems can be overcome by surveying only when there is good weather and illumination, i.e. daytime, with no rain, but neither with direct sunlight (Cook, 2017; Crawford et al., 2018; Mlambo et al., 2017; Morocho et al., 2019; Vanneschi et al., 2017). One example of the problems because of the weather conditions was the campaign corresponding to December. The UAV surveys were developed between 9 and 10 am to avoid shadows from the midday sun, and afternoon winds. However, on the December 3rd, it was a sunny day from the early hours, reducing the contrast of the images, shadow creating occlusion zones, gaps, and irregular geometries on the UAV-SfM derived products. The survey had to be replaced by a new survey on December 20th. That one erroneous campaign produced a significant non-homogeneity between the periods of time analyzed.

In recent years, UAV-SfM techniques have been highly utilized for many different field applications. Many of them related to the field of geology, to geomorphic change detection applications such as mining (Guiseppe et al., 2017; Peterson et al., 2015), landslide monitoring (N. Ahmad et al., 2018; Giuseppe Esposito et al., 2017; Sanz et al., 2018; Terra, 2016), rock fall (Rocca, 2020), gully erosion (Cândido et al., 2020; Slimane et al., 2018), sea cliff (Barlow et al., 2017), coastal dune (Duffy et al., 2018), bedrock surfaces (Cook, 2017), fluvial surface (Williams et al., 2020), wetlands (Boon et al., 2016), moraine complex (M. J. Westoby et al., 2016), drifting icebergs and ice islands (Crawford et al., 2018), among others.

c Also, to avoid any changing of the procedure applied in the Phase 3, because differences in the procedure in each UAV campaign and TS survey can falsify the results, i.e., obtain incorrect data of the movements and deformation of the slope.

In this case study, given that the aerial photogrammetry surveys and the post-processing of the data do not obtain the same resolution even though they were executed in the same modality, the GSD is probably affected by external factors such as the wind or the weak GPS signal, accentuating the dome effect. In our study we implemented GCPs to reduce the propagation of systemic errors of the dome effect in the reconstruction of the models. However, some authors have suggested that the SfM techniques do not require any type of ground control points (Niethammer et al., 2010).

We feel that UAV photogrammetry needs to be complemented with traditional topography or similar techniques to ensure correct alignment of point clouds and surface models obtained with SfM software, as well as to validate the measurements of the point clouds and multi-temporal surface reconstruction approach in a global georeferenced system. One way to do this is to use GCPs which increase the aligning efficiency of the images. Additionally, it is less time consuming, since no additional manual addition of markers or extra manual matching of images is needed. UAV-SfM method can be carried out without the use of Ground Control Points. However, we utilized GCPs accurately located with Trimble Total Station to directly assess the goodness of the UAV based ground movement analysis.

RMSE may reduce as more and more accurate GCPs are used. The resulting RMS with only 6 ground control points, located on one side of the study area, provided errors in a range of 2.81 to 1.44 m. However, when using 21 GCPs distributed throughout the study area, the error is between 0.21 to 0.16 m. The use of the ICP alignment tool available on Cloud Compare software can significantly reduce absolute positional accuracy (N. Ahmad et al., 2018; Lague et al., 2013; Moghaddmane-Jafari, 2016; Rocca, 2020). This further emphasizes the flexible operation of UAV surveys with a minor number of GCPs.

The classification and automatic removal of vegetation, buildings, noise, and any non-surface points provided by the CANUPO algorithm at a 98% of effectivity (Brodu & Lague, 2012) allowed a validation of the results obtained by C2M and M3C2 point cloud distance comparison. In comparison to existing techniques and algorithms such as C2M method, the M3C2 simplify and improve the comparison of the point clouds, but also allowed us to detect statistically significant changes on rough surfaces. The performance of C2M, by the interpolation over missing data introduces uncertainties that are difficult to quantify. The C2M can be as accurate as the M3C2, but M3C2 offers values over a spatially variable of confidence while C2M absolute values of difference. Furthermore, other advantages are the following:

- a) There is no meshing or gridding needed for the point cloud with the M3C2 algorithm. It is important because the mesh reconstruction smooths out some details provided by the point cloud data.
- b) If there are data gaps (e.g, shadows due to sun, removal of vegetation etc.) the C2M creates overestimates (Cook, 2017; Girardeau-Montaut et al., 2005). On the contrary the M3C2 algorithm does not compute distances along the normal direction when faced with data gaps in order to avoid introducing errors on the calculations (Figure 10). This is clearly shown in the results section, since the displacement observed in the southern profile does not correctly estimate the M3C2 results, but there is an overestimation in the C2M. This is especially true for natural landscapes where rough morphology may lead to missing data, and interpolation errors are difficult to quantify (e.g., Wheaton et al. 2010; Heritage et al. 2009).

In summary M3C2 is more appropriate for the spatial analysis of UAV-SfM data from complex terrains. It is better when faced with changes in point density as well as point cloud noise than C2M (Lague et al., 2013). In a related study, by Barnhart and Crosby (2013) analyzed surface change detection with both methods. They successfully proved that the M3C2 method provides better results in displacement measurement compared to C2M method where M3C2 manages to calculate the true horizontal displacements while C2M could not, but nevertheless managed to pass the threshold of change detection.

The normal scale (D) is particularly important on the M3C2 process for complex terrains. This parameter needs to be large enough to not be affected by the rough surface, as mentioned in the methods section. The preliminary results of C2M, distances observed in the profiles, and the 3D vectors displacement were also considered, allowing to determine a D equal to 2 m. M3C2 can be applied to any type of terrain. However, the greatest benefit of it is with rough surfaces derived from complex terrains where a confidence interval (LOD95%) of achieved changes can be incorporated. The LOD95% can be used to estimate the accuracy of the local distance measurement changes given the co-registration error, surface roughness and point cloud density. Furthermore, LOD95% is beneficial as it indirectly shows the locations of remaining vegetation points as these will have higher LOD95% values than the other points around it (Lague et al., 2013).

The estimation of the 3D vectors of motion was satisfactory, even though this complementary study was not intended to be carried out at first. The results could not be corroborated with others obtained in the present study since the M3C2 results were calibrated with a confidence interval of 9 cm, and the profiles do not cross through any of the control point locations. However, consistent values such as horizontal and vertical displacements, with their respective azimuths corresponding to the observed displacements, reflect the veracity of the results. In addition, as they are direct results of the traditional topography survey, it has only the manufactured error of the method (Direct Refraction), which using the Trimble Total Station S5 is +/- 2 mm.

The complex interaction between with removal and deposition occurring simultaneously in the area (Suárez, 2009), make it difficult to measure and quantify the morphological changes along

the whole area. Based on changes on slope geometry the profiles represent two dimensional morphological changes on the most critical areas of both faces of the study area. This information mainly allowed us to estimate the optimal value for the normal scale for the M3C2 process, where we could observe changes of up to 2 m in the South profile, however these values are not considered as significant changes for the M3C2 results.

Most slopes are apparently stable and static, but they are actually evolving dynamic systems. (Suárez, 2009). The processes that occur on a slope are generally complex and depend on many factors, which interact with each other to define a behavior. Therefore, some of the factors involved allow us to discern their behavior. If the diagnosis is wrong, remedial measures or stabilization procedures fail. Prior to the design of remedial measures, one must have a knowledge of the magnitude of the damage, the causes and the mechanisms that generate it. Especially in the soils of volcanic deposits, where the homogeneity of the material and the variety of the fundamental parameters make the deterministic analysis imprecise.

The fundamental elements to study the stability of a slope are lithology and geological formation, geological structure, geomorphology, state of weathering, tectonic and fracture slope, topography, climate and hydrology, seismicity, vegetation, the anthropic effect, the time factor, probability of the triggering factors, evolution of movements and remedial alternatives. For this type of study, knowledge of geology, soil mechanics, hydrology, morphology, and environmental characteristics of the site, among other fundamental elements, is required. The behavior of the slopes depends on the characteristics of the geomorphology of the sector, this reflects the processes that are acting on the slope, as well as the paleo processes that have affected it in the past.

- a) Steepness of slope. The relief is a determining factor in the stability of a slope, although not necessarily it is more unstable if the slope is greater. However, as the slope increases, the forces that try to destabilize the slope are generally increased. Steep slopes are very susceptible to landslides, drops, and waste streams. The area corresponding to the construction of the City of knowledge Yachay, has restrictions on the execution of any civil works in the Regular Type III geotechnical classification area. This classification comprises areas with reliefs with significantly steep slopes and morphological processes,

such as ravines, colluvial, high hills of volcanic origin, low terraces, and alluvial valleys. The limit to this area is not more than 500 meters from our study area, and since there is no other geotectonic study available, this information has been taken into account (Ecuambiente, 2014).

- b) Lithology (primary volcanic deposits denominated as poorly cohesive soils). The primary volcanic materials are characterized by being poorly consolidated. The unconsolidated material is susceptible to collapse resulting in slope failure (Suárez, 2009).
- c) An additional contribution of water in the wet season. The effect of precipitation and ground water level on landslides and land movements is not always straightforward and has proven to be fairly difficult to study (Brückl et al., 2006). However, the changing slope conditions play a determinant role in the stability of the slope. The main mechanism that contributes to instability is the elevation of the phreatic level due to the net infiltration of water, resulting in an increase in the specific weight of the land. Also, precipitation increases the pore pressure of the soil particles, which affects the loss cohesion and resistance to friction. Exceptional rains in semi-arid areas generate additional and accelerated problems of erosion and mass movements. Unfortunately, we did not collect data during the dry season. However, the data presented show that when the precipitations are higher (October and November) the displacements in some areas increase.
- d) Anthropogenic activities; dumping of fill material or waste on the ravine. In a stable slope there is a balance between the acting forces and the resisting forces, among which the force of gravity is the most determining. If additional loads are placed on the top of the slope or removed at the foot, new instabilities may occur. Likewise, changes in the shape of the slope can affect the instability of the slope. Some of the anthropic processes that affect the stability of the slopes are the following: the fillings or deposits of materials on the slope, waste disposal, water leaks from the service networks, artificial vibrations, traffic of vehicles, which generate dynamic forces and the deterioration of the structure of the materials. In general, the movement of land to create more space for building in areas where the soil are not well consolidated is promoting further slope destabilization. In this case, in

January material was removed in the stable zone (Figure #), three mounds of waste material with dimensions of approximately 3m² were dumped into the ravine.

- e) Existing slope failures and a rotational landslide. Some large mass movements correspond to old movements, which have been reactivated or are still in motion. A landslide is the movement downhill of a soil or rock mass that occurs predominantly on well-defined breaking surface or on relatively narrow areas of intense shear (Cruden & Varnes, 1996).

For these reasons, it is crucial to know the factors involved in slope failure processes and understand the interactions between them, so that the area's most susceptible to failure can be identified and the mitigation, and correction can be implemented. In general, any external process should be considered for its influence on the slope behavior. Most of the processes that affect the stability of a slope do not occur instantaneously, but rather generally take long periods of time. On an apparently stable slope, many unnoticed phenomena may be occurring leading to a failure.

In Ecuador, 35% of the population lives in areas threatened by various phenomena of moving material such as mudslides, landslides, and erosion, triggered mainly by intense rainfall. The lack of government regulation results in frequent construction of buildings in marginal areas of very high risk, which increases the degree of vulnerability. Review the cartographic information on mass movements related hazards in the town of Urcuquí compiled by the Ecuadorian Secretariat for Risk Management, it is observed that there is a high level of many types of mass movements. Some buildings are located close to terrains with slopes of 40 degrees with poorly cohesive soils. Despite this, the Municipal Autonomous Decentralized Government of San Miguel of Urcuquí does not have a contingency plan to respond to any natural and man-made disasters (GADMU, 2015). Unfortunately, there is no regulatory entity in Ecuador that controls or requests preliminary studies of the areas where any type of infrastructure will be built. Therefore, the lack of government regulations results in frequent construction of buildings in marginal areas of very high risk, which increases the degree of vulnerability.

CONCLUSIONS

UAV photogrammetry data processed with SfM software's provide high accuracy products for spatial analysis of instability areas. This research aimed to describe numerically the morphology changes over time to assess the behavior of the slope failure kinematics. The results highlight the advantages of UAV-SfM technique to detect and interpreted morphological changes in rough surfaces over time. One major advantage of UAV photogrammetry application to hazardous environments is the possibility to obtain periodical measurements and secure monitoring from a distance. Compared with traditional techniques methodology based on UAV platforms reduces the working time and avoids the risk when the study site is dangerous. However, it is not possible to reach the resolution of millimeters which was obtained to describe the 3D vectors motion, where a total station was used. Results of the C2M and M3C2 comparisons supported the analysis, the measurements shown critical regions of constant movement and slope failure in the two sides of the ravine in which the study was developed. This study opens new possibilities in the development of control strategies and monitoring of the of slope instability areas. This approach can be also considered as source of accurate information to manage disaster risks related to slope processes as well as for planning for land use. For example, increasing the knowledge of the spatial and temporal behavior of areas prone to slope failure can help avoid human settlements being built on potential slope instability areas on the surroundings growth area of Urcuquí city.

REFERENCES

- Agüera, F., Carvajal, F., & Martínez, P. (2017). Assessment of photogrammetric mapping accuracy based on variation ground control points number using unmanned aerial vehicle. *Measurement: Journal of the International Measurement Confederation*, *98*, 221–227. <https://doi.org/10.1016/j.measurement.2016.12.002>
- Ahmad, N., Yusoff, A., Ismail, Z., & Majid, Z. (2018). Comparing the performance of point cloud registration methods for landslide monitoring using mobile laser scanning data. *International Archives of the Photogrammetry, Remote Sensing and Spatial Information Sciences - ISPRS Archives*, *42(4/W9)*, 11–21. <https://doi.org/10.5194/isprs-archives-XLII-4-W9-11-2018>
- Ahmad, Z. A., Guey, C. W., Sze, L. T., & Chet, K. V. (2017). Scalable and cost effective high resolution digital elevation model extraction method for slope's stability assessment. *Advanced Science Letters*, *23(2)*, 1289–1293. <https://doi.org/10.1166/asl.2017.8367>
- Arif, F., Abdul Maulud, K. N., & Ab Rahman, A. A. (2018). Generation of digital elevation model through aerial technique. *IOP Conference Series: Earth and Environmental Science*, *169(1)*. <https://doi.org/10.1088/1755-1315/169/1/012093>
- Barlow, J., Gilham, J., & Ibarra Cofrã, I. (2017). Kinematic analysis of sea cliff stability using UAV photogrammetry. *International Journal of Remote Sensing*, *38(8–10)*, 2464–2479. <https://doi.org/10.1080/01431161.2016.1275061>
- Beate, B., & Urquizo, M. (2015). Geothermal country update for Ecuador, 2010–2015. *Proceedings World Geothermal Congress Melbourne, Australia., April*, 19–25.
- Boon, M. A., Greenfield, R., & Tesfamichael, S. (2016). Unmanned Aerial Vehicle (UAV) photogrammetry produces accurate high-resolution orthophotos, point clouds and surface models for mapping wetlands. *South African Journal of Geomatics*, *5(2)*, 186. <https://doi.org/10.4314/sajg.v5i2.7>
- Borgatti, L., Vittuari, L., & Zanutta, A. (2010). *Geomatic methods for punctual and areal control of surface changes due to landslide phenomena. Landslides: Causes, Types and Effects*. Nova Science Publishers Inc.
- Brodu, N., & Lague, D. (2012). 3D terrestrial lidar data classification of complex natural scenes using a multi-scale dimensionality criterion: Applications in geomorphology. *ISPRS Journal*

- of *Photogrammetry and Remote Sensing*, 68(1), 121–134.
<https://doi.org/10.1016/j.isprsjprs.2012.01.006>
- Brückl, E., Brunner, F. K., & Kraus, K. (2006). Kinematics of a deep-seated landslide derived from photogrammetric, GPS and geophysical data. *Engineering Geology*, 88(3–4), 149–159.
<https://doi.org/10.1016/j.enggeo.2006.09.004>
- Cândido, B. M., James, M., Quinton, J., Lima, W. de, & Silva, M. L. N. (2020). Sediment source and volume of soil erosion in a gully system using UAV photogrammetry. *Revista Brasileira de Ciência Do Solo*, 44, 1–14. <https://doi.org/10.36783/18069657rbcS20200076>
- Cao, L., Liu, H., Fu, X., Zhang, Z., Shen, X., & Ruan, H. (2019). Comparison of UAV LiDAR and digital aerial photogrammetry point clouds for estimating forest structural attributes in subtropical planted forests. *Forests*, 10(2), 1–26. <https://doi.org/10.3390/f10020145>
- Cook, K. L. (2017). An evaluation of the effectiveness of low-cost UAVs and structure from motion for geomorphic change detection. *Geomorphology*, 278, 195–208.
<https://doi.org/10.1016/j.geomorph.2016.11.009>
- Crawford, A. J., Mueller, D., & Joyal, G. (2018). Surveying drifting icebergs and ice islands: Deterioration detection and mass estimation with aerial photogrammetry and laser scanning. *Remote Sensing*, 10(4). <https://doi.org/10.3390/rs10040575>
- Delgado, A. (2016). *Comparación de nube de puntos obtenidas mediante laser 3D y sistemas estereoscópicos ópticos*. 76.
- Duffy, J. P., Shutler, J. D., Witt, M. J., DeBell, L., & Anderson, K. (2018). Tracking fine-scale structural changes in coastal dune morphology using kite aerial photography and uncertainty-assessed structure-from-motion photogrammetry. *Remote Sensing*, 10(9).
<https://doi.org/10.3390/rs10091494>
- Ecuambiente. (2014). *RESUMEN EJECUTIVO DEL ESTUDIO DE IMPACTO AMBIENTAL DEL PROYECTO DE LA CIUDAD DEL CONOCIMIENTO “YACHAY.”*
<https://maeimbabura.files.wordpress.com/2014/06/eia-yachay.pdf>
- Eker, R., Aydın, A., & Hübl, J. (2018). Unmanned aerial vehicle (UAV)-based monitoring of a landslide: Gallenzerkogel landslide (Ybbs-Lower Austria) case study. *Environmental Monitoring and Assessment*, 190(1). <https://doi.org/10.1007/s10661-017-6402-8>
- Esposito, Giuseppe, Salvini, R., Matano, F., Sacchi, M., Danzi, M., Somma, R., & Troise, C. (2017). Multitemporal monitoring of a coastal landslide through SfM-derived point cloud

- comparison. *Photogrammetric Record*, 32(160), 459–479.
<https://doi.org/10.1111/phor.12218>
- Esposito, Guisepe, Mastrorocco, G., Salvini, R., Oliveti, M., & Starita, P. (2017). Application of UAV photogrammetry for the multi-temporal estimation of surface extent and volumetric excavation in the Sa Pigada Bianca open-pit mine, Sardinia, Italy. *Environmental Earth Sciences*, 76(3). <https://doi.org/10.1007/s12665-017-6409-z>
- GADMU. (2015). *Actualización del Plan de Desarrollo y Ordenamiento Territorial San Miguel de Urucuquí* (Vol. 2015, p. 127).
- Girardeau-Montaut, D., Roux, M., Marc, R., & Thibault, G. (2005). Change Detection on Points Cloud Data Acquired With a Ground. *International Archives of Photogrammetry Remote Sensing and Spatial Information Sciences*, 36(part 3), 30–35.
http://www.danielgm.net/phd/isprs_laserscanning_2005_dgm.pdf
- Gobierno Provincial de Imbabura. (2015). *Actualización Del Plan De Ordenamiento Territorial De La Provincia De Imbabura 2015-2035*. http://app.sni.gob.ec/sni-link/sni/PORTAL_SNI/data_sigad_plus/sigadplusdocumentofinal/1060000180001_PDOT_IMBABURA_2015-2035_SIGAD_15-08-2015_22-50-42.pdf
- He, L., & Heki, K. (2018). Three-Dimensional Tomography of Ionospheric Anomalies Immediately Before the 2015 Illapel Earthquake, Central Chile. *Journal of Geophysical Research: Space Physics*, 123(5), 4015–4025. <https://doi.org/10.1029/2017JA024871>
- Hugenholtz, C. H., Walker, J., Brown, O., & Myshak, S. (2015). Earthwork Volumetrics with an Unmanned Aerial Vehicle and Softcopy Photogrammetry. *Journal of Surveying Engineering*, 141(1), 06014003. [https://doi.org/10.1061/\(asce\)su.1943-5428.0000138](https://doi.org/10.1061/(asce)su.1943-5428.0000138)
- INEC. (2010). *Censo de Población y Vivienda 2010*. <https://www.ecuadorencifras.gob.ec/home-prueba-poblacion-y-migracion/>
- James, M. R., Robson, S., & Smith, M. W. (2017). 3-D uncertainty-based topographic change detection with structure-from-motion photogrammetry: precision maps for ground control and directly georeferenced surveys. *Earth Surface Processes and Landforms*, 42(12), 1769–1788. <https://doi.org/10.1002/esp.4125>
- Kameyama, S., & Sugiura, K. (2021). Effects of differences in structure from motion software on image processing of unmanned aerial vehicle photography and estimation of crown area and tree height in forests. *Remote Sensing*, 13(4), 1–22. <https://doi.org/10.3390/rs13040626>

- Kazhdan, M., Bolitho, M., & Hoppe, H. (2006). Poisson Surface Reconstruction. *Eurographics Symposium on Geometry Processing*, 7, 525–537. https://doi.org/10.1007/978-3-319-18461-6_42
- Kerle, N., Nex, F., Gerke, M., Duarte, D., & Vetrivel, A. (2019). UAV-based structural damage mapping: A review. *ISPRS International Journal of Geo-Information*, 9(1), 1–23. <https://doi.org/10.3390/ijgi9010014>
- Lague, D., Brodu, N., & Leroux, J. (2013). Accurate 3D comparison of complex topography with terrestrial laser scanner: Application to the Rangitikei canyon (N-Z). *ISPRS Journal of Photogrammetry and Remote Sensing*, 82, 10–26. <https://doi.org/10.1016/j.isprsjprs.2013.04.009>
- Mlambo, R., Woodhouse, I. H., Gerard, F., & Anderson, K. (2017). Structure from motion (SfM) photogrammetry with drone data: A low cost method for monitoring greenhouse gas emissions from forests in developing countries. *Forests*, 8(3). <https://doi.org/10.3390/f8030068>
- Moghaddmane-Jafari, B. (2016). *Deflection Measurement Through 3D Point Cloud Analysis*. George Mason University.
- Morocho, V., España, D. A., Serrano, A. C., Achig, R., & Cromptoets, J. (2019). Mass movements detection from uav images analysis. *International Archives of the Photogrammetry, Remote Sensing and Spatial Information Sciences - ISPRS Archives*, 42(2/W13), 461–467. <https://doi.org/10.5194/isprs-archives-XLII-2-W13-461-2019>
- Nex, F., & Remondino, F. (2014). UAV for 3D mapping applications: A review. *Applied Geomatics*, 6(1), 1–15. <https://doi.org/10.1007/s12518-013-0120-x>
- Niethammer, U., Rothmund, S., James, M. R., Travelletti, J., Joswig, M., & Centre, L. E. (2010). *Uav-Based Remote Sensing of Landslides*. XXXVIII(2005).
- Nieto Masot, A., Navazo Arenas, G., & Moreno Marcos, G. (2016). Tecnologías de la información geográfica en el análisis espacial: aplicaciones en los sectores público, empresarial y universitario. In *Tecnologías de la Información Geográfica en el Análisis Espacial. Aplicaciones en los Sectores Público, Empresarial y Universitario, 2016*, ISBN 978-84-617-6760-1, págs. 247-268. <https://dialnet.unirioja.es/servlet/articulo?codigo=5776243>
- Peterson, E., Klein, M., & Stewart, R. (2015). Constructing Three Dimensional Models from Photography. In *US Department of Interior Bureau of Reclamation Research and*

- Development Office (Issue October).*
https://www.researchgate.net/publication/308106693_Whitepaper_on_Structure_from_Motion_on_SfM_Photogrammetry_Constructing_Three_Dimensional_Models_from_Photography
- Preston, R. P. (2021). Implementation of a Pit Slope-Monitoring Network for Inactive Open-Pit Mines Using Photogrammetry. *Rock Mechanics and Rock Engineering*, 0123456789. <https://doi.org/10.1007/s00603-021-02417-y>
- Rocca, A. La. (2020). *A photogrammetry application to rockfall monitoring: the Belca, Slovenia case study.*
- Sanz, E., Chandler, J., Rodríguez, J., & Ordóñez, C. (2018). Accuracy of Unmanned Aerial Vehicle (UAV) and SfM photogrammetry survey as a function of the number and location of ground control points used. *Remote Sensing*, 10(10). <https://doi.org/10.3390/rs10101606>
- Shenzhen DJI Sciences and Technologies Ltd. (2021). *DJI*. <https://www.dji.com/inspire-2/info>
- Slimane, A. Ben, Raclot, D., Rebai, H., Le Bissonnais, Y., Planchon, O., & Bouksila, F. (2018). Combining field monitoring and aerial imagery to evaluate the role of gully erosion in a Mediterranean catchment (Tunisia). *Catena*, 170(December 2017), 73–83. <https://doi.org/10.1016/j.catena.2018.05.044>
- Stöcker, C., Eltner, A., & Karrasch, P. (2015). Measuring gullies by synergetic application of UAV and close range photogrammetry - A case study from Andalusia, Spain. *Catena*, 132, 1–11. <https://doi.org/10.1016/j.catena.2015.04.004>
- Suárez, J. (2009). Capítulo 2. Mecanismos de falla. In *Deslizamientos: Análisis geotécnico* (pp. 37–74).
- Terra, S. Della. (2016). *Semi-automatic analysis of landslide spatio-temporal evolution.*
- Trimble Geospatial*. (n.d.). Retrieved June 7, 2021, from <https://geospatial.trimble.com/products-and-solutions/trimble-s5>
- UNDESA. (2016). The World’s Cities in 2016 – Data Booklet (ST/ESA/ SER.A/392). *United Nation*, 8(6), 8557–8571.
- Vanneschi, C., Eyre, M., Francioni, M., & Coggan, J. (2017). The Use of Remote Sensing Techniques for Monitoring and Characterization of Slope Instability. *Procedia Engineering*, 191, 150–157. <https://doi.org/10.1016/j.proeng.2017.05.166>
- Westoby, M., Brasington, J., Glasser, N., Hambrey, M., & Reynolds, J. (2012). “Structure-from-Motion” photogrammetry: A low-cost, effective tool for geoscience applications.

Geomorphology, 179, 300–314. <https://doi.org/10.1016/j.geomorph.2012.08.021>

- Westoby, M. J., Dunning, S. A., Woodward, J., Hein, A. S., Marrero, S. M., Winter, K., & Sugden, D. E. (2016). Interannual surface evolution of an Antarctic blue-ice moraine using multi-temporal DEMs. *Earth Surface Dynamics*, 4(2), 515–529. <https://doi.org/10.5194/esurf-4-515-2016>
- Williams, R. D., Lamy, M. Lou, Maniatis, G., & Stott, E. (2020). Three-dimensional reconstruction of fluvial surface sedimentology and topography using personal mobile laser scanning. *Earth Surface Processes and Landforms*, 45(1), 251–261. <https://doi.org/10.1002/esp.4747>
- Zapata, A., Zapata, J., Ordoñez, E., Hugonieto, V., & Viniachi, F. (2019). Lineamientos generales socioeconómicos para una propuesta de ordenamiento territorial de la cabecera cantonal de San Miguel de Urququí, Ecuador. *Revista de Ciencias de Seguridad y Defensa*, 4(8), 71–126. <http://geol.espe.edu.ec/wp-content/uploads/2019/02/6art8.pdf>

ANNEXES

Annexe 1: Quality report of UAV images postprocessing corresponding to October on Pix4D Mapper software.

Quality Report



Generated with Pix4Dmapper version 4.5.6

- !** **Important:** Click on the different icons for:
 - ?** Help to analyze the results in the Quality Report
 - i** Additional information about the sections

Click [here](#) for additional tips to analyze the Quality Report

Summary i

Project	01-Oct-20
Processed	2021-05-12 12:22:36
Camera Model Name(s)	FC6510_8.8_5472x3648 (RGB)(1), FC6510_8.8_5472x3648 (RGB)(2), FC6510_8.8_5472x3648 (RGB)(3)
Average Ground Sampling Distance (GSD)	4.03 cm / 1.59 in
Area Covered	0.158 km ² / 15.7902 ha / 0.06 sq. mi. / 39.0387 acres

Quality Check i

? Images	median of 86406 keypoints per image	
? Dataset	553 out of 553 images calibrated (100%), 1 images disabled	
? Camera Optimization	0.63% relative difference between initial and optimized internal camera parameters	
? Matching	median of 24887.6 matches per calibrated image	
? Georeferencing	yes, 3D GCP	

? Preview i

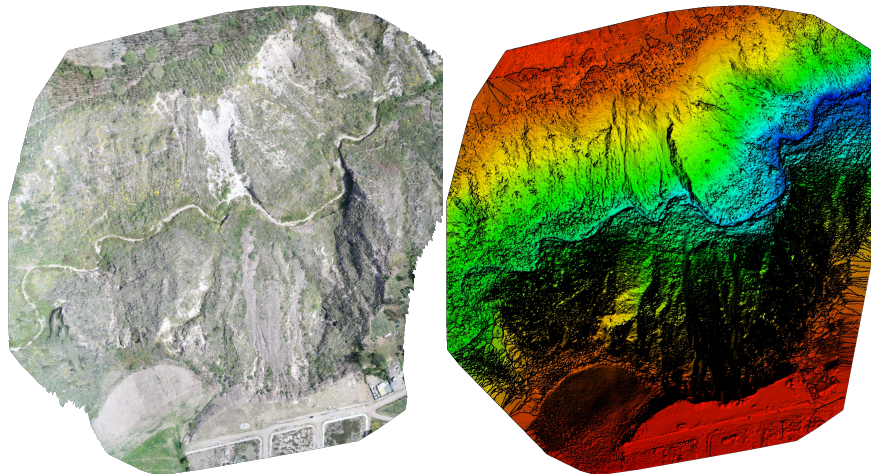


Figure 1: Orthomosaic and the corresponding sparse Digital Surface Model (DSM) before densification.

Calibration Details



Number of Calibrated Images	553 out of 554
Number of Geolocated Images	554 out of 554

? Initial Image Positions

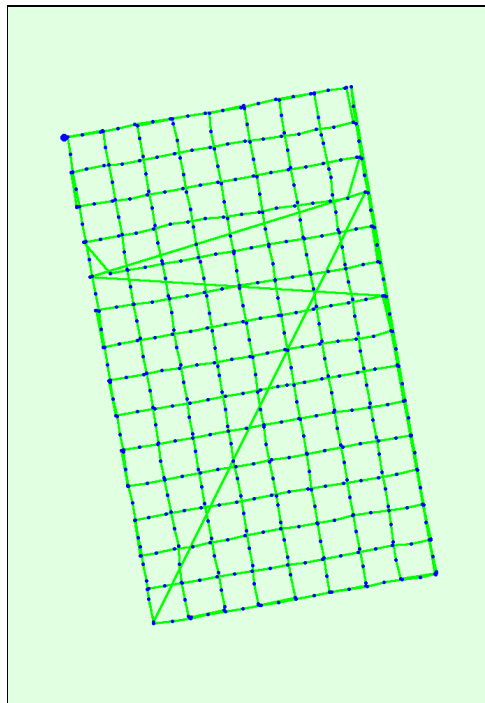
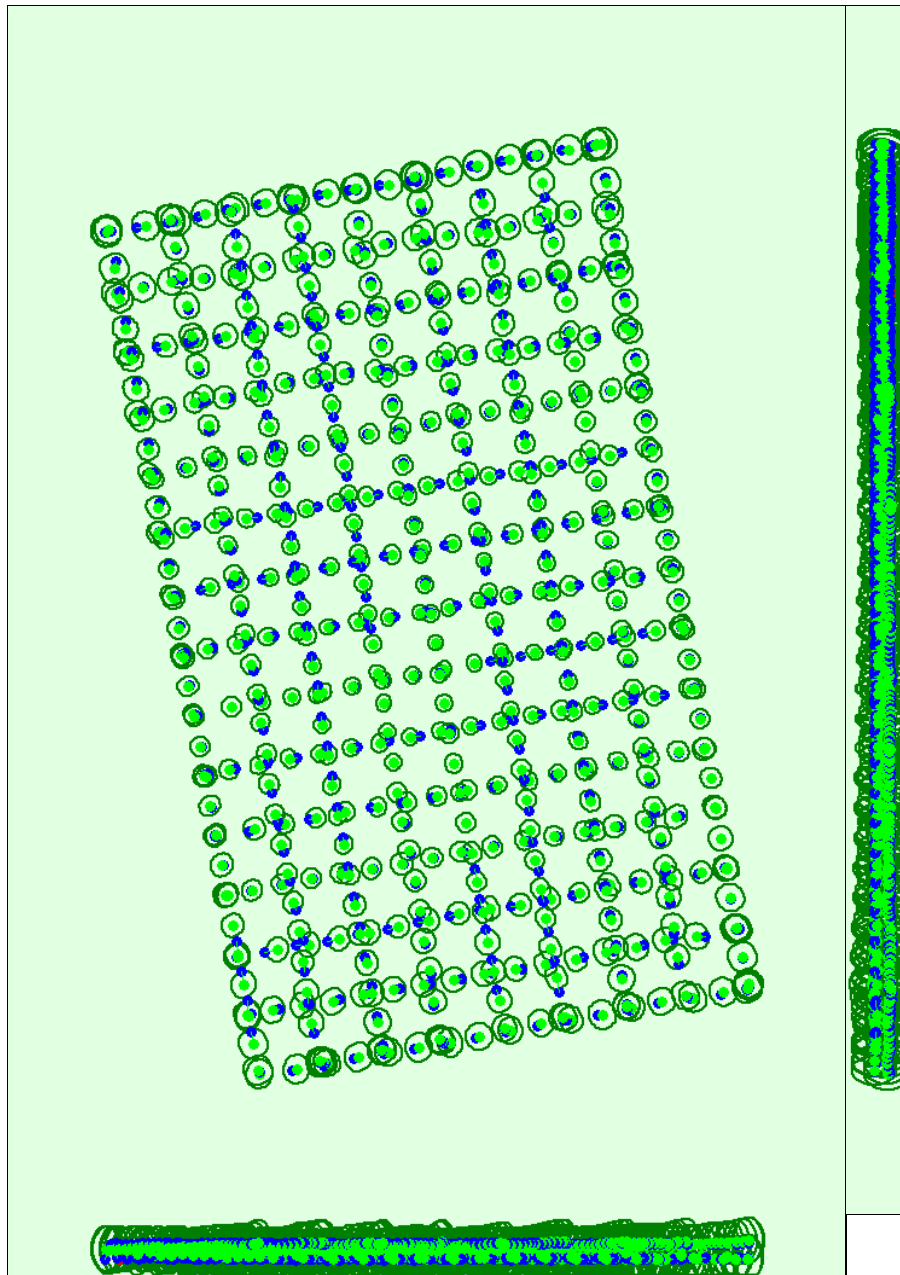


Figure 2: Top view of the initial image position. The green line follows the position of the images in time starting from the large blue dot.

? Computed Image/GCPs/Manual Tie Points Positions





Uncertainty ellipses 50x magnified

Figure 3: Offset between initial (blue dots) and computed (green dots) image positions as well as the offset between the GCPs initial positions (blue crosses) and their computed positions (green crosses) in the top-view (XY plane), front-view (XZ plane), and side-view (YZ plane). Red dots indicate disabled or uncalibrated images. Dark green ellipses indicate the absolute position uncertainty of the bundle block adjustment result.

🔍 Absolute camera position and orientation uncertainties



	X[m]	Y[m]	Z[m]	Omega [degree]	Phi [degree]	Kappa [degree]
Mean	0.085	0.087	0.145	0.035	0.038	0.028
Sigma	0.013	0.014	0.012	0.000	0.000	0.000

Overlap

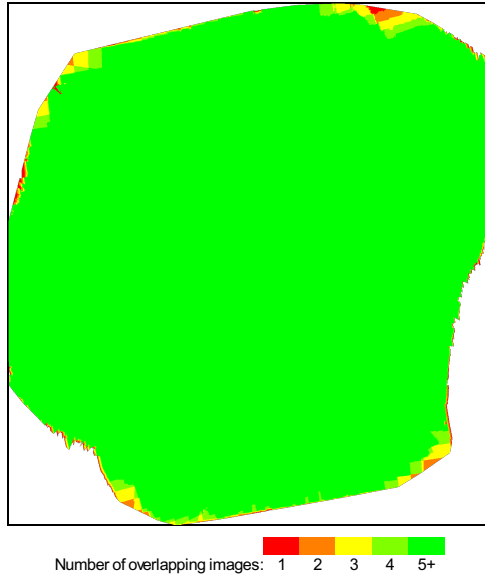


Figure 4: Number of overlapping images computed for each pixel of the orthomosaic. Red and yellow areas indicate low overlap for which poor results may be generated. Green areas indicate an overlap of over 5 images for every pixel. Good quality results will be generated as long as the number of keypoint matches is also sufficient for these areas (see Figure 5 for keypoint matches).

Bundle Block Adjustment Details



Number of 2D Keypoint Observations for Bundle Block Adjustment	13421309
Number of 3D Points for Bundle Block Adjustment	4082382
Mean Reprojection Error [pixels]	0.132

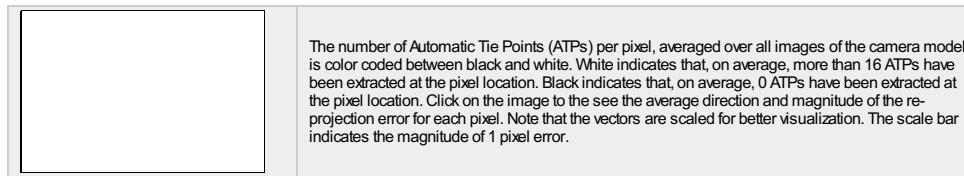
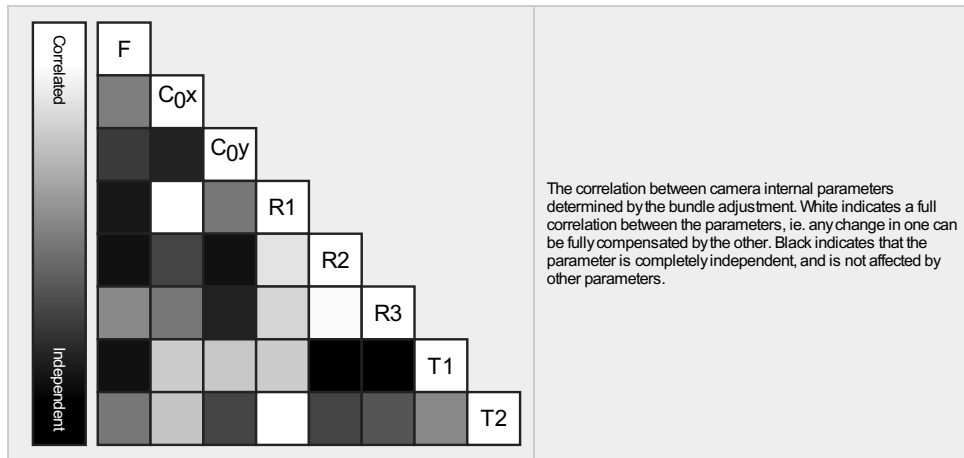
Internal Camera Parameters

FC6510_8.8_5472x3648 (RGB)(1). Sensor Dimensions: 12.833 [mm] x 8.556 [mm]



EXIF ID: FC6510_8.8_5472x3648

	Focal Length	Principal Point x	Principal Point y	R1	R2	R3	T1	T2
Initial Values	3689.447 [pixel] 8.653 [mm]	2730.905 [pixel] 6.405 [mm]	1829.687 [pixel] 4.291 [mm]	0.003	-0.011	0.011	0.001	0.001
Optimized Values	3662.069 [pixel] 8.589 [mm]	2744.826 [pixel] 6.437 [mm]	1849.080 [pixel] 4.337 [mm]	0.004	-0.017	0.015	0.001	0.002
Uncertainties (Sigma)	0.564 [pixel] 0.001 [mm]	0.060 [pixel] 0.000 [mm]	0.039 [pixel] 0.000 [mm]	0.000	0.000	0.000	0.000	0.000

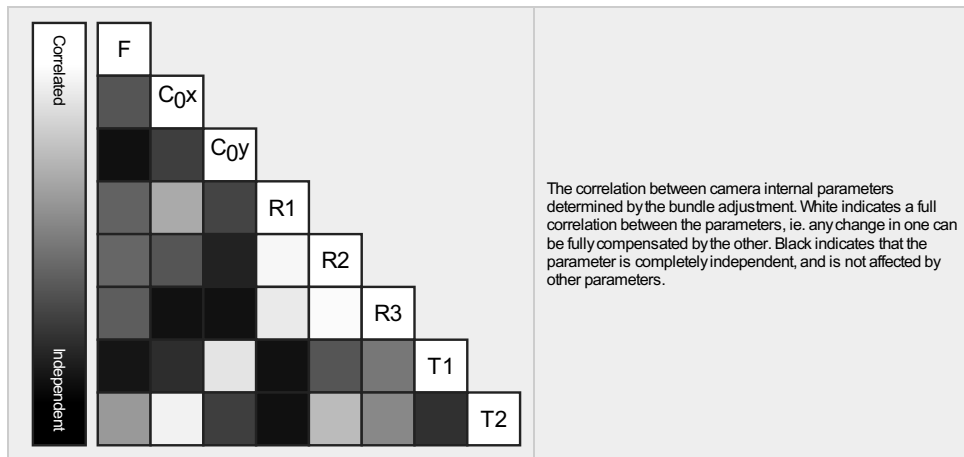


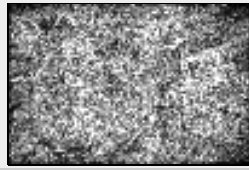
Internal Camera Parameters

FC6510_8.8_5472x3648 (RGB)(2). Sensor Dimensions: 12.833 [mm] x 8.556 [mm]

EXIF ID: FC6510_8.8_5472x3648

	Focal Length	Principal Point x	Principal Point y	R1	R2	R3	T1	T2
Initial Values	3689.447 [pixel] 8.653 [mm]	2730.905 [pixel] 6.405 [mm]	1829.687 [pixel] 4.291 [mm]	0.003	-0.011	0.011	0.001	0.001
Optimized Values	3666.860 [pixel] 8.600 [mm]	2743.598 [pixel] 6.434 [mm]	1851.548 [pixel] 4.342 [mm]	0.007	-0.021	0.019	0.001	0.002
Uncertainties (Sigma)	0.862 [pixel] 0.002 [mm]	0.808 [pixel] 0.002 [mm]	0.719 [pixel] 0.002 [mm]	0.001	0.003	0.003	0.000	0.000





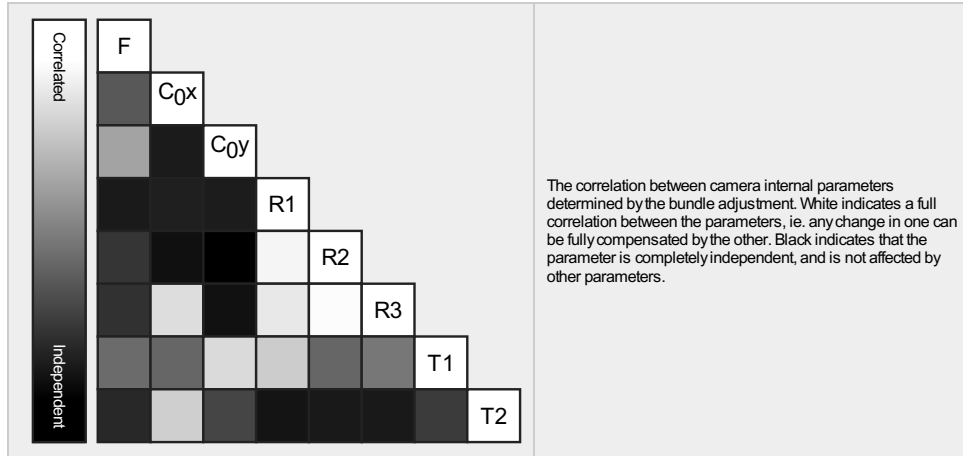
The number of Automatic Tie Points (ATPs) per pixel, averaged over all images of the camera model, is color coded between black and white. White indicates that, on average, more than 16 ATPs have been extracted at the pixel location. Black indicates that, on average, 0 ATPs have been extracted at the pixel location. Click on the image to see the average direction and magnitude of the re-projection error for each pixel. Note that the vectors are scaled for better visualization. The scale bar indicates the magnitude of 1 pixel error.

Internal Camera Parameters

FC6510_8.8_5472x3648 (RGB)(3). Sensor Dimensions: 12.833 [mm] x 8.556 [mm]

EXIF ID: FC6510_8.8_5472x3648

	Focal Length	Principal Point x	Principal Point y	R1	R2	R3	T1	T2
Initial Values	3689.447 [pixel] 8.653 [mm]	2730.905 [pixel] 6.405 [mm]	1829.687 [pixel] 4.291 [mm]	0.003	-0.011	0.011	0.001	0.001
Optimized Values	3669.130 [pixel] 8.605 [mm]	2746.215 [pixel] 6.441 [mm]	1849.326 [pixel] 4.337 [mm]	0.010	-0.033	0.033	0.001	0.002
Uncertainties (Sigma)	2.059 [pixel] 0.005 [mm]	1.557 [pixel] 0.004 [mm]	1.441 [pixel] 0.003 [mm]	0.002	0.006	0.006	0.000	0.000



The number of Automatic Tie Points (ATPs) per pixel, averaged over all images of the camera model, is color coded between black and white. White indicates that, on average, more than 16 ATPs have been extracted at the pixel location. Black indicates that, on average, 0 ATPs have been extracted at the pixel location. Click on the image to see the average direction and magnitude of the re-projection error for each pixel. Note that the vectors are scaled for better visualization. The scale bar indicates the magnitude of 1 pixel error.

2D Keypoints Table

	Number of 2D Keypoints per Image	Number of Matched 2D Keypoints per Image
Median	86406	24888
Min	60388	5075
Max	89891	39781
Mean	81912	24270

2D Keypoints Table for Camera FC6510_8.8_5472x3648 (RGB)(1)

	Number of 2D Keypoints per Image	Number of Matched 2D Keypoints per Image
Median	86414	24916
Min	60388	5075

Max	89891	39781
Mean	81959	24308

2D Keypoints Table for Camera FC6510_8.8_5472x3648 (RGB)(2)

	Number of 2D Keypoints per Image	Number of Matched 2D Keypoints per Image
Median	76672	29162
Min	70916	8540
Max	86611	29162
Mean	77124	17950

2D Keypoints Table for Camera FC6510_8.8_5472x3648 (RGB)(3)

	Number of 2D Keypoints per Image	Number of Matched 2D Keypoints per Image
Median	75776	0
Min	75776	28549
Max	75776	28549
Mean	75776	28549

Median / 75% / Maximal Number of Matches Between Camera Models

	FC6510_8.8_5...(RGB)(1)	FC6510_8.8_5...(RGB)(2)	FC6510_8.8_5...(RGB)(3)
FC6510_8.8_5472x3648 (RGB)(1)	35 / 195 / 27106	39 / 257 / 18872	51 / 244 / 18263
FC6510_8.8_5472x3648 (RGB)(2)		837 / (n/a) / 837	236 / (n/a) / 2365
FC6510_8.8_5472x3648 (RGB)(3)			

3D Points from 2D Keypoint Matches



	Number of 3D Points Observed
In 2 Images	2304604
In 3 Images	818093
In 4 Images	370343
In 5 Images	194004
In 6 Images	113286
In 7 Images	72297
In 8 Images	48412
In 9 Images	34162
In 10 Images	25068
In 11 Images	18711
In 12 Images	14422
In 13 Images	11125
In 14 Images	8765
In 15 Images	7249
In 16 Images	5726
In 17 Images	4880
In 18 Images	4021
In 19 Images	3440
In 20 Images	2941
In 21 Images	2363
In 22 Images	2214
In 23 Images	1829
In 24 Images	1577
In 25 Images	1437
In 26 Images	1153
In 27 Images	1024
In 28 Images	934
In 29 Images	763
In 30 Images	712
In 31 Images	632

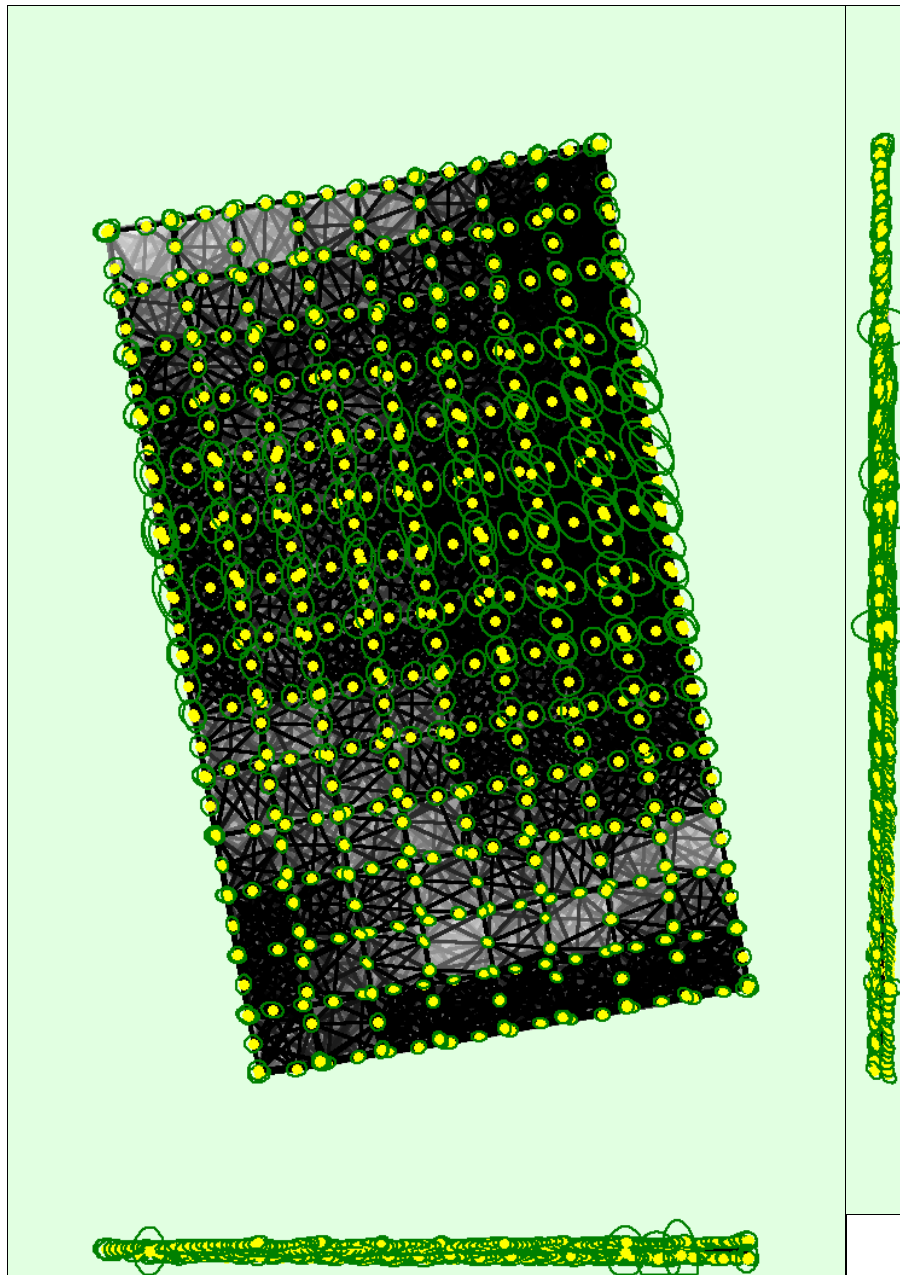
In 32 Images	533
In 33 Images	504
In 34 Images	439
In 35 Images	383
In 36 Images	337
In 37 Images	278
In 38 Images	292
In 39 Images	232
In 40 Images	216
In 41 Images	202
In 42 Images	158
In 43 Images	173
In 44 Images	146
In 45 Images	163
In 46 Images	134
In 47 Images	131
In 48 Images	126
In 49 Images	104
In 50 Images	104
In 51 Images	104
In 52 Images	92
In 53 Images	70
In 54 Images	83
In 55 Images	71
In 56 Images	69
In 57 Images	51
In 58 Images	61
In 59 Images	45
In 60 Images	45
In 61 Images	38
In 62 Images	36
In 63 Images	33
In 64 Images	39
In 65 Images	41
In 66 Images	33
In 67 Images	24
In 68 Images	35
In 69 Images	17
In 70 Images	30
In 71 Images	22
In 72 Images	26
In 73 Images	16
In 74 Images	19
In 75 Images	12
In 76 Images	18
In 77 Images	15
In 78 Images	21
In 79 Images	22
In 80 Images	12
In 81 Images	17
In 82 Images	11
In 83 Images	9
In 84 Images	9
In 85 Images	12
In 86 Images	8
In 87 Images	8
In 88 Images	10
In 89 Images	5
In 90 Images	9

In 91 Images	8
In 92 Images	7
In 93 Images	9
In 94 Images	6
In 95 Images	4
In 96 Images	11
In 97 Images	7
In 98 Images	9
In 99 Images	5
In 100 Images	4
In 101 Images	5
In 102 Images	9
In 103 Images	9
In 104 Images	7
In 105 Images	6
In 106 Images	6
In 107 Images	3
In 108 Images	6
In 109 Images	5
In 110 Images	6
In 111 Images	4
In 112 Images	4
In 113 Images	2
In 114 Images	1
In 116 Images	4
In 117 Images	2
In 118 Images	1
In 119 Images	2
In 120 Images	1
In 121 Images	1
In 122 Images	2
In 123 Images	5
In 124 Images	3
In 125 Images	2
In 126 Images	6
In 127 Images	2
In 128 Images	2
In 129 Images	4
In 130 Images	3
In 131 Images	1
In 132 Images	1
In 133 Images	1
In 134 Images	2
In 135 Images	1
In 136 Images	3
In 137 Images	1
In 138 Images	1
In 139 Images	1
In 140 Images	2
In 142 Images	3
In 143 Images	3
In 144 Images	2
In 145 Images	1
In 146 Images	2
In 147 Images	1
In 149 Images	2
In 151 Images	1
In 152 Images	1
In 153 Images	2

In 154 Images	2
In 157 Images	1
In 158 Images	1
In 164 Images	1
In 167 Images	2
In 169 Images	1
In 170 Images	1
In 173 Images	1
In 174 Images	1
In 180 Images	1
In 182 Images	1
In 184 Images	1
In 185 Images	1
In 187 Images	1
In 188 Images	1
In 189 Images	1
In 190 Images	1
In 191 Images	1
In 196 Images	1
In 199 Images	1
In 205 Images	1
In 211 Images	1
In 235 Images	1
In 240 Images	1
In 249 Images	1

 **2D Keypoint Matches**





Uncertainty ellipses 500x magnified

Number of matches

25 222 444 666 888 1111 1333 1555 1777 2000

Figure 5: Computed image positions with links between matched images. The darkness of the links indicates the number of matched 2D keypoints between the images. Bright links indicate weak links and require manual tie points or more images. Dark green ellipses indicate the relative camera position uncertainty of the bundle block adjustment result.

Relative camera position and orientation uncertainties



X[m]	Y[m]	Z[m]	Omega [degree]	Phi [degree]	Kappa [degree]
------	------	------	----------------	--------------	----------------

Mean	0.008	0.009	0.005	0.005	0.004	0.002
Sigma	0.003	0.004	0.002	0.001	0.001	0.000

Geolocation Details

? Absolute Geolocation Variance

Min Error [m]	Max Error [m]	Geolocation Error X[%]	Geolocation Error Y[%]	Geolocation Error Z[%]
-	-15.00	0.00	0.00	0.00
-15.00	-12.00	0.00	0.00	0.00
-12.00	-9.00	0.00	0.00	0.00
-9.00	-6.00	0.00	0.00	0.00
-6.00	-3.00	7.96	7.23	2.71
-3.00	0.00	38.34	42.68	50.99
0.00	3.00	49.01	42.31	45.57
3.00	6.00	4.70	7.78	0.72
6.00	9.00	0.00	0.00	0.00
9.00	12.00	0.00	0.00	0.00
12.00	15.00	0.00	0.00	0.00
15.00	-	0.00	0.00	0.00
Mean [m]		-0.000013	0.000037	0.000154
Sigma [m]		1.765309	1.911744	1.446740
RMS Error [m]		1.765309	1.911744	1.446740

Min Error and Max Error represent geolocation error intervals between -1.5 and 1.5 times the maximum accuracy of all the images. Columns X, Y, Z show the percentage of images with geolocation errors within the predefined error intervals. The geolocation error is the difference between the initial and computed image positions. Note that the image geolocation errors do not correspond to the accuracy of the observed 3D points.

? Relative Geolocation Variance

Relative Geolocation Error	Images X[%]	Images Y[%]	Images Z[%]
[-1.00, 1.00]	98.92	97.65	100.00
[-2.00, 2.00]	100.00	100.00	100.00
[-3.00, 3.00]	100.00	100.00	100.00
Mean of Geolocation Accuracy [m]	5.000000	5.000000	10.000000
Sigma of Geolocation Accuracy [m]	0.000000	0.000000	0.000000

Images X, Y, Z represent the percentage of images with a relative geolocation error in X, Y, Z.

Geolocation Orientational Variance	RMS [degree]
Omega	1.874
Phi	1.604
Kappa	4.826

Geolocation RMS error of the orientation angles given by the difference between the initial and computed image orientation angles.

Initial Processing Details

System Information

Hardware	CPU: Intel(R) Core(TM) i7-7700 CPU @ 3.60GHz RAM: 8GB GPU: Intel(R) HD Graphics 630 (Driver: 27.20.100.8681), Radeon RX550/550 Series (Driver: 27.20.1034.6)
Operating System	Windows 10 Pro, 64-bit

Coordinate Systems i

Image Coordinate System	WGS 84 (EGM96 Geoid)
Output Coordinate System	WGS 84 / UTM zone 17N (EGM96 Geoid)

Processing Options i

Detected Template	No Template Available
Keypoints Image Scale	Full, Image Scale: 1
Advanced: Matching Image Pairs	Aerial Grid or Corridor
Advanced: Matching Strategy	Use Geometrically Verified Matching: no
Advanced: Keypoint Extraction	Targeted Number of Keypoints: Automatic
Advanced: Calibration	Calibration Method: Standard Internal Parameters Optimization: All External Parameters Optimization: All Rematch: Auto, no

Point Cloud Densification details i

Processing Options i

Image Scale	multiscale, 1/2 (Half image size, Default)
Point Density	Optimal
Minimum Number of Matches	2
3D Textured Mesh Generation	no
LOD	Generated: no
Advanced: Image Groups	group1
Advanced: Use Processing Area	yes
Advanced: Use Annotations	yes

Results i

Number of Generated Tiles	4
Number of 3D Densified Points	48205898
Average Density (per m ³)	109.79

DSM, Orthomosaic and Index Details i

Processing Options i

DSM and Orthomosaic Resolution	1 x GSD (4.03 [cm/pixel])
DSM Filters	Noise Filtering: yes Surface Smoothing: yes, Type: Sharp
Orthomosaic	Generated: yes Merge Tiles: yes GeoTIFF Without Transparency: no Google Maps Tiles and KML: no
Grid DSM	Generated: yes, Spacing [cm]: 5

Annexe 1: Comparison report of the CGPs located on the front part of the study area

Project file data		Coordinate System	
Name:	C:\Users\DELL\Desktop\Results Trimble Business Center\Point comparison report	Name:	Por defecto
Size:	72 KB	Datum:	WGS 1984
Modified:	21/5/2021 16:05:57	Zone:	17 N
Time zone:	UTC:-5	Geoide:	
Reference number:	2	Vertical datum:	
Description:	GCPs comparison report	Calibrated site:	
Comment 1:	Data from 18-Jan-2021		
Comment 2:	Data to 06-Feb-2021		
Comment 3:			

Point comparison report

Horizontal range:	0,200 m	Horizontal tolerance:	0,020 m
Vertical range:	0,200 m	Vertical tolerance:	0,050 m

From	To	Δ Horizontal	Azimuth	Δ East	Δ North	Δ Vertical
1J	1JM	0,004 m	276°57'11"	-0,004 m	0,001 m	-0,002 m
1J	F	0,009 m	308°33'30"	-0,007 m	0,006 m	-0,003 m
1J	FM	0,010 m	306°45'33"	-0,008 m	0,006 m	-0,003 m
1J	M	0,014 m	320°30'32"	-0,009 m	0,011 m	-0,036 m
2J	2F	0,005 m	344°21'28"	-0,001 m	0,005 m	-0,013 m
2J	2FM	0,007 m	332°21'14"	-0,003 m	0,006 m	-0,020 m
2J	2JM	0,004 m	347°28'16"	-0,001 m	0,004 m	-0,009 m
2J	2M	0,012 m	324°37'31"	-0,007 m	0,010 m	-0,031 m
3J	3F	0,002 m	322°25'53"	-0,001 m	0,001 m	-0,021 m
3J	3FM	0,003 m	321°04'21"	-0,002 m	0,003 m	-0,038 m
3J	3JM	0,001 m	315°00'00"	-0,001 m	0,001 m	-0,006 m
3J	3M	0,007 m	301°15'49"	-0,006 m	0,003 m	-0,059 m
4J	4F	0,035 m	236°59'49"	-0,029 m	-0,019 m	-0,172 m
4J	4FM	0,067 m	243°26'06"	-0,060 m	-0,030 m	-0,242 m
4J	4JM	0,019 m	261°13'51"	-0,019 m	-0,003 m	-0,007 m
5J	5F	0,005 m	302°13'44"	-0,005 m	0,003 m	-0,005 m
5J	5FM	0,013 m	287°19'41"	-0,013 m	0,004 m	-0,022 m
5J	5JM	0,003 m	331°41'57"	-0,001 m	0,003 m	-0,003 m
5J	5M	0,032 m	287°25'05"	-0,031 m	0,010 m	-0,034 m
6J	6F	0,020 m	211°35'21"	-0,011 m	-0,017 m	-0,017 m
6J	6FM	0,026 m	220°14'11"	-0,017 m	-0,020 m	-0,030 m
6J	6JM	0,009 m	190°21'33"	-0,002 m	-0,009 m	-0,014 m

6J	M	0,041 m	226°35'28"	-0,030 m	-0,028 m	-0,051 m
----	---	---------	------------	----------	----------	----------

21/5/2021 16:09:11	C:\Users\DELL\Desktop\Resuls Trimble Business Center\Point comparison report	Trimble Business Center
--------------------	--	-------------------------